Synergistic Voltage and Electrolyte Mediation Improves Sodiation Kinetics in µ-Sn Alloy-anodes

Abstract

Alloying electrodes, such as tin (Sn), are promising candidates for sodium-ion batteries because of their high specific capacity, electronic conductivity, and low sodium insertion voltage. However, sizeable volumetric change and electrode-electrolyte interface evolution in Sn preclude prolonged performance. The electrochemical potential window, compounded by the choice of electrolyte and additive combination, plays a critical role in the interface instability which yet remains unresolved. This study, based on a comprehensive set of electrochemical, microscopy and spectroscopic analyses, sheds light into the interface instability and reveals that the use of fluoroethylene carbonate additives in carbonate-based electrolytes can dramatically improve the interface stability of such alloying anodes. Electrochemical and morphological analyses show that without the additive, a higher end-of-charge voltage can cause breakdown and reformation of an unstable passivating layer, leading to rapid electrochemical performance decay. A novel three-electrode-based analytics reveals that superior interphase stability with higher microstructural integrity of the Sn electrode can alleviate the detriments from the upper cut-off voltage restrictions. Addressing the hitherto unresolved role of the electrochemical potential window, this study comprehensively examines and elucidates the causality of interfacial instability and the underpinnings of electrochemical complexations in sodium-alloying anodes.

Keywords: sodium-ion battery, alloying electrode, electrochemical and interface instability, carbonate electrolyte

1. Introduction

While the lithium-ion batteries (LIBs) are the current *de facto* franchise for appeasing the fast-growing exigency for portable energy storage devices, *de jure*, other chemistries such as sodium-ion batteries (SIBs) are gaining a positive momentum towards establishing a promising alternative in large-scale grid energy storage because of their ubiquitousness, and striking similarities with LIB chemistry. The relevant thermodynamic, kinetic, and transport properties fare advantageously or disadvantageously for the SIBs due to the wider ionic size, the less convenient redox potential of Na^+, and different bonding characteristics. This entails constraint into Na intercalation and leads to a restricted selection of electrode materials. For instance, graphite, a popular anode in LIBs, is an outcast in SIBS due to the fundamental discrepancy between Na^+ ionic radius of ≈1.02 nm and graphite interlayer distance of ≈0.334 nm. Past studies have focused on morphological tailoring or formulating 'non-graphitizing' carbons to either bypass or cleave the bottleneck. [1–4] Nevertheless, most of these studies, along with many others, consummated that these carbonaceous materials only possess specific charge-discharge capacities around 200–300 mAh/g with limited rate capability and poor cycling stability, even with the complex fabrication process and expensive electrolyte additives.[5–12]

Due to the limited capacity of carbonaceous material, alloy-based electrodes (e.g., Si, Sn, etc.) are quite popular because of their higher theoretical specific capacity. Past studies have identified volume expansion with higher shear stress and cracks, disconnection/pulverization of active material as one of the root causes of electrochemical instability, which makes Sn undesirable for prolonged use.[13–16] Usage of active bi/tri-metallic alloys Sn-Sb,[17,18] Sn-Bi-Sb,[19] Sn-P[20–22], and active- electrochemically inert alloys such as Sn-Co,[23] Sn-Ni,[24] Sn-Fe[25] have been one of the commonly used approaches to elevate cycling stability besides high specific capacity. Utilizing composite Sn electrode structures by introducing new physio-chemical properties to improve cycling capability increases the material/production cost, which can be eased by using elemental micro-Sn particles in a tailored electrochemical condition.

In addition to the electrode material, the design of a stable electrolyte composition is essential as the upgrowth of the electrode-electrolyte interface during the electrochemical reaction process dominates the electrode integrity and reversibility of battery cycling by preventing parasitic side reactions. Understanding the physio-chemical properties and rational design of the electrode-electrolyte interface is a long-pursued task for the battery

community.[26–28] Given the vacuousness of pure Sn electrode response and microstructural changes of electrode-electrolyte interface layer during stable and metastable phase change events, cycling performances are often vaguely described. Although previous studies have shown the dependency of the phase sequence with terminal cut-off voltages, the possibility for cut-off voltage optimization for robust electrode-electrolyte interface remains unrecognized.[29,30]

This paper studied the evolution of the electrode-electrolyte interface during different electrochemical conditions with different charge-discharge protocols. Carbonate-based electrolytes (e.g., EC, PC, DMC, EMC, DEC, etc.) in the presence of additives (FEC, VC) are standard for exerting efficient and reversible performance in LIBs.[31–34] By leveraging LIB's knowledge, before seeking an ideal electrolyte for SIBs, it is imperative to understand how carbonates react with anode material for effective passivation.[28] Thus, carbonate-based electrolytes, PC and PC: FEC, were picked as the electrolytes for these sets of experiments. Deterioration mechanism of Sn-based sodium-ion battery and microstructural change during charge-discharge cycle tests in restricted terminal voltages was investigated thoroughly in this work. The impact of upper and lower cut-off limits on kinetic hindrance caused by slower ionic diffusion and charge transfer resistance has been discussed in detail. Comprehensively, this study addresses the following research gaps: a) the reversibility of oxidation and reduction peaks of Na_xSn for different charge cut-off voltage, b) the reversibility of electrode reactions at different C-rates, c) the morphological and structural change of Sn skeletons; and d) the evolution of electrode surface in different electrolyte cocktails.

2. Results and discussion

Electrochemical and morphological analysis of Sn anodes with PC electrolyte

Electrode potential is one of the most powerful tools in electrochemistry controlled by experimentalists to change the position of thermodynamics equilibria and reaction rates (kinetics). During the sodiation-desodiation process, electrode potential varies through the multi-step reactions in the Sn anode. To better grasp equilibrium phase transition behavior, the battery is discharged at a rate slow enough for Na to form an alloy, adopting a distinct crystal structure during intermediate steps involving multiphase reactions. Aqueously processed micro-Sn-based porous electrodes were charged-charged at a slow rate of C/25 and C/100 (**Figure S1**). Although the plateaus are seen at slightly different voltages for different C-rates, the profile of potential curves is the same. The voltage plateaus observed at a C/100 shifts down

to a lower value at C/100 (e.g., 0.4061 v to 0.3211 V at discharge, 0.13 V to 0.16 V at a charge) mainly due to overpotential buildup on the electrode at higher current density. Thus, the usage of lower current density is recommended to better understand the capacity degradation mostly originated from the active material loss. As is measured, the four plateaus could be assigned to four electrochemical reactions. Plateaus I, II, and III contribute most of the desodiation capacity of the Sn anode during the charging process. The plateaus are more distinct during the desodiation process than sodiation, indicating that the average time of phase transformation time for individual Sn crystallites is relatively slower than that of Na-rich Sn alloy. Besides, the side reactions between the active material and electrolyte resulted in a higher capacity than the theoretical value (847 mAh/g) at a low current density of C/100. The lower current rate caused a longer reaction time and extra Na consumption with the SEI layer formation.

To explore the cut-off voltage influence on the electrochemical properties, cycling performances, and the charge-discharge profiles were compared. We have selected 0.7V, 0.8V, 1.2V, and 1.6 V as our target end-off charge voltage for the property evolution. **Figure 1** presents the schematic and SEM images of all the processed electrodes with evolved electrode-electrolyte "interface" layer. A significant change in the interface morphology has been observed. We can see the presence of a thick 'dry-mud' type passivation layer composed of both organic and inorganic compounds for 0.7 and 0.8 V cases.[35] At low potential (< 0.4 V), Na_xSn reaction phases occur and cause an unrestrictive reductive breakdown of electrolyte species on the fresh anode surface. Continuous bloating and diminution of the Sn particles related to Na alloying and de-alloying cause the passivation layer to rupture locally. The renewed, highly reactive electrode surface is again unmasked to the electrolyte, leaving a thicker layer. As we keep increasing the charge voltage of 1.6V, a wafer-thin passivation layer has been observed. The absence of a thicker passivation layer is inept at avoiding the uninviting, ill-favored, and undoable reaction of the anode with electrolyte, which grows on nonstop feasting of both Na and electrolyte. This passivation layer is also adversely affecting coulombic efficiency (CE), shown in **Figure 1(b)**. A denser layer leads to extraneous electrolyte decomposition and Na ion loss with continuous cycling, decreasing the CE. **Figure 1(c)** shows the cycling performances for 20 cycles. Compared with the 1.6 V cut-off voltage, the 0.7 and 0.8V cut-off voltage gives significantly better capacity retention for the long run. 0.7V, 0.8V, and 1.2V cut-off voltage have a similar capacity in the first few cycles at 0.1 C. However, when a higher C-rate (0.5C) was used, 0.7 and 0.8V had much better capacity retention than 1.2V, primarily due to minor mechanical damage from limited Na alloying/de-

alloying. The thick passivation at lower voltage buffers the inevitable volume expansion of the Sn anode upon Na alloying even at higher rates and avoids significant delamination and cracking of the electrode, displaying improvement in cycling stability.

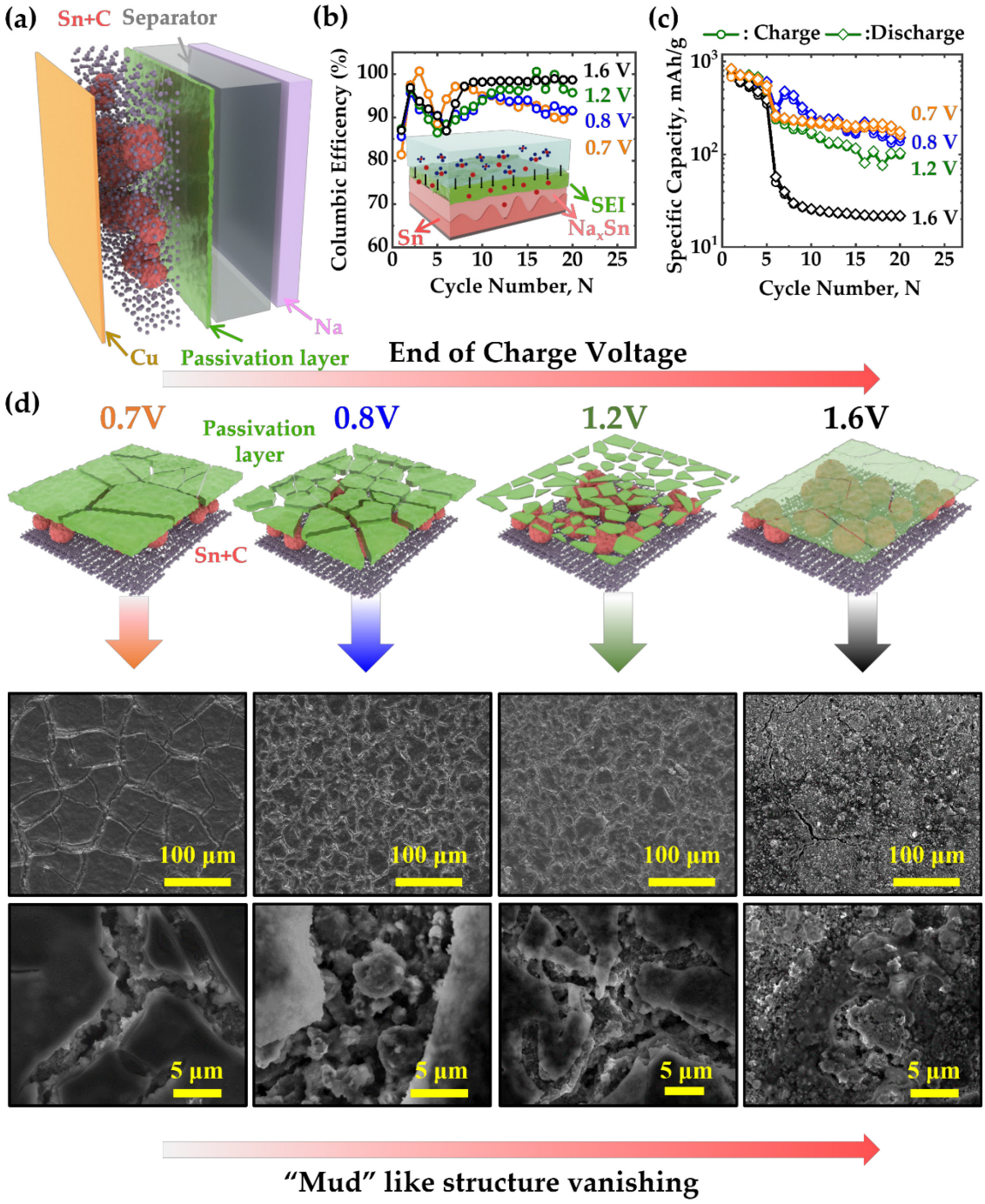

Figure 1. Effect of end of charge voltage on cycle performance. The test cells were discharged and charged at constant current at 0.1C-rate to different cut-off voltages for the first 5 cycles and then at 0.5C for the subsequent 15 cycles. (a) Schematic of a Na-Sn cell, (b) Coulombic efficiency, (c) Specific capacity vs. cycle number, and (d) Evolution of anode-electrolyte

interphase (schematic and SEM image) for different end of charge voltages. The electrolyte was $NaClO_4$:PC.

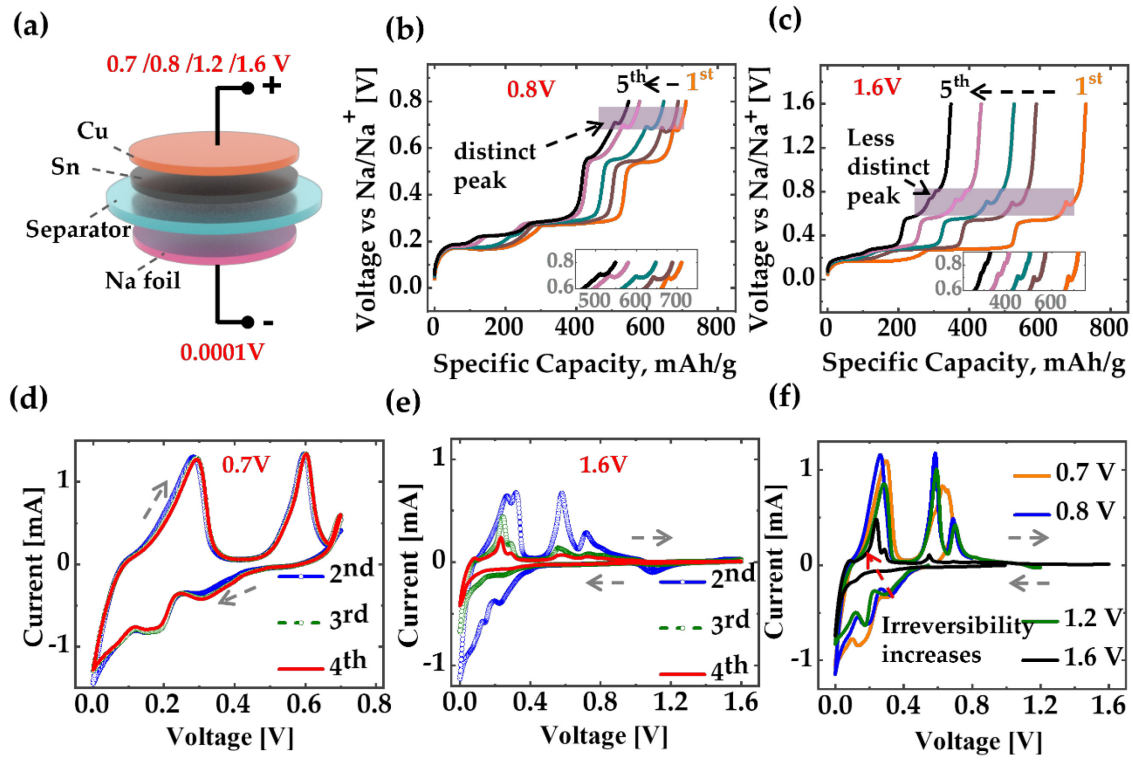

Figure 2. (a) The test cells (Sn-Na cells) were discharged and charged to different cut-off voltages. The first 5 charge profiles for (b) 0.8 V and (c) 1.6 V. Inset shows the zoomed-in charge profiles to clearly identify the peak between 0.6V and 0.8V. Cyclic voltammetry (CV) curves of fresh Sn-Na cells at different cut-off voltages. (d) 0.8V, and (e) 1.6V. (f) CV of cycled Sn-Na cells. This CV test was done after one constant current cycle (charge-discharge) at different cut-off voltages.

Figure 2(a) shows the typical coin cell system and different potential windows used in this study. To thoroughly investigate the impact of cut-off voltage, the first five charge profiles were plotted for 0.8 V and 1.6 V voltage in **Figures 2b** and **2c**. It is evident from the 2nd cycle that 1.6 V had much more capacity fading than the other three voltages. During sodiation/desodiation, Na-Sn can exist in several phases at room temperature, such as Sn, $NaSn_3$, NaSn, Na_9Sn_4, $Na_{15}Sn_4$ (**Figure S1**). Kinetic limitation causes always-observed large hysteresis in the sodium insertion/de-insertion process as well as less distinct plateaus with cycling, indicating further changes in intermediated phases. **Figure S2** shows that the charging up to 1.2 V alters the subsequent charge profile indicating that the reaction might have taken a

different reaction pathway. A significant observation is that of flattening of the plateaus, which implies less favorable kinetics for the phase changes. For instance, a 0.68 V plateau that is present at the 1st cycle diminishes with further cycling at 1.6V. However, 1.6 V has a similar first charge-discharge capacity as 0.7 V because pure Sn is always covered with a thin oxide layer which prevents significant electrolyte decomposition at the first cycle. **Figure S2(c)** shows the discharge profiles for all the cases. The reduction peaks are less sharp for all the instances than oxidation peaks, indicating the slower reaction kinetics of alloying than de-alloying. The inset of **Figure S2(c)** shows that except for 0.7 V, all the other cases follow the same reaction path. The results reveal that the restricting charge cut-off to lower voltage is significant to avoid the anomalous irreversible reaction on the anode.

Figures 2(d)-(e) and **S3** compare the cyclic voltammograms of the Sn electrode in different potential scanning ranges. A broad reduction peak around 0.22 V is observed during the first cathodic scan, which can be credited to the formation of solid-electrolyte interphase (SEI) film. Two small reduction peaks at 0.19 V and 0.06 are allocated to the sodium intercalation into Sn to make a Na_xSn alloy. Oxidation peaks at 0.19, 0.34, 0.58, and 0.7 V correspond to the desodiation reaction of Na_xSn alloy. In the potential range between 0.8 and 0.0001V, two reduction peaks have shifted at 0.3V and 0.19V in the second cycle. Also, the oxidation peak at 0.19V has disappeared, and a pair of peaks at 0.27 and 0.31 V have been formed. All peaks are reversible after the second cycle, denoting decent cycling stability at 0.8V charge cut-off voltage. While the range was restricted to 1.2V, the oxidation pair peak disappeared in the second cycle, and a peak of 0.33V was formed. While the charge cut-off was restricted to 1.6V, in the first cycle additional small peak was seen at 1.48V, and the oxidation peak at 0.27 and 0.32V re-appeared in the second cycle. However, the reversibility of the peaks became poor. Besides, at 1.6 V charge cut-off voltage, the cathodic peaks change to lesser voltages, while the anodic peaks move to upper voltages, signifying a higher charge-discharge polarization and deterioration of the reaction kinetics. In **Figure 2(f)**, the cells were subjected to cyclic voltammetry (CV) test after one cycle of charge-discharge at 0.1C-rate. 1.6 V shows very poor reversibility suggesting poor cell performance. The desodiation peaks mainly diminish in size as we keep increasing the voltage. Thus, the CV results back up the galvanostatic cycling data obtained in different voltage ranges.

Electrochemical impedance spectroscopy (EIS) measures the impedance variations of an electrochemical system subjected to a voltage applied in sinusoidal perturbations. Information about structural changes of the electrode upon cycling can be determined from

EIS. **Figure S4(a)** shows the EIS spectra of the pristine electrode (at OCP of ~2.7 V), and the electrodes cycled in the different voltage windows of 1.6, 1.2, 0.8, and 0.7V. The impedance parameters for the cycled electrode and fresh electrode are fitted by using the equivalent circuits in **Figures S4 (b)-(c).** As seen from Figure, there are primarily two arcs in the high frequency and medium frequency domain. While the high-frequency arc is due to the SEI layer formation, the medium frequency arc is due to the charge transfer resistance, and they can be modeled using a resistor (R_{SEI} or R_{ct}) and constant phase element (CPE) in parallel. In the equivalent circuit, Z_d represents the finite length diffusion element, which is represented by:

$$\boldsymbol{Z_d(f) = R_d \frac{\coth{(\tau_d j 2\pi f)^{\alpha/2}}}{(\tau_d j 2\pi f)^{\alpha/2}}}.$$

Where $\boldsymbol{\tau_d}$ is the diffusion time constant, and α is the dispersion parameter.

R_s, which depends on the ionic conductivity of the electrolyte solution, was determined to be around 4 Ω for all the cases. For the pristine electrode before cycling, the Nyquist plot has a semi-circle and an oblique line. With the activation of the electrode, Nyquist plots for the cycled electrode at 0.7V and 0.8V consist of two superposed depressed semi-circles in the high and medium frequency zones and an oblique line, respectively. After near complete extraction at 1.2 V and 1.6 V, the spectrum displayed well-defined high frequency and medium-frequency arcs. The significant amount of Na extraction at 0.68 V during desodiation can be a possible reason behind the absence of the medium frequency arc for impedance measurement at 0.7V and 0.8V. **Figure S4(d)** shows how the resistances change with different potential windows. R_{ct}, the charge transfer resistance, was observed to increase during Na extraction, which can be linked to changes in surface area and electronic conductivity of the active material. The SEI layer resistance (R_{SEI} is lowest for 1.6 V, as charging up to that high voltage led to frequent SEI break-and-repair healing processes and thus leading to the thinner SEI layer. As the upper cut-off voltage is increasing, contraction of the active particles due to extensive Na extraction is severe, which causes the detrimental fracturing of the existing SEI layer and promotes the development of thin film on a fresh electrode surface.

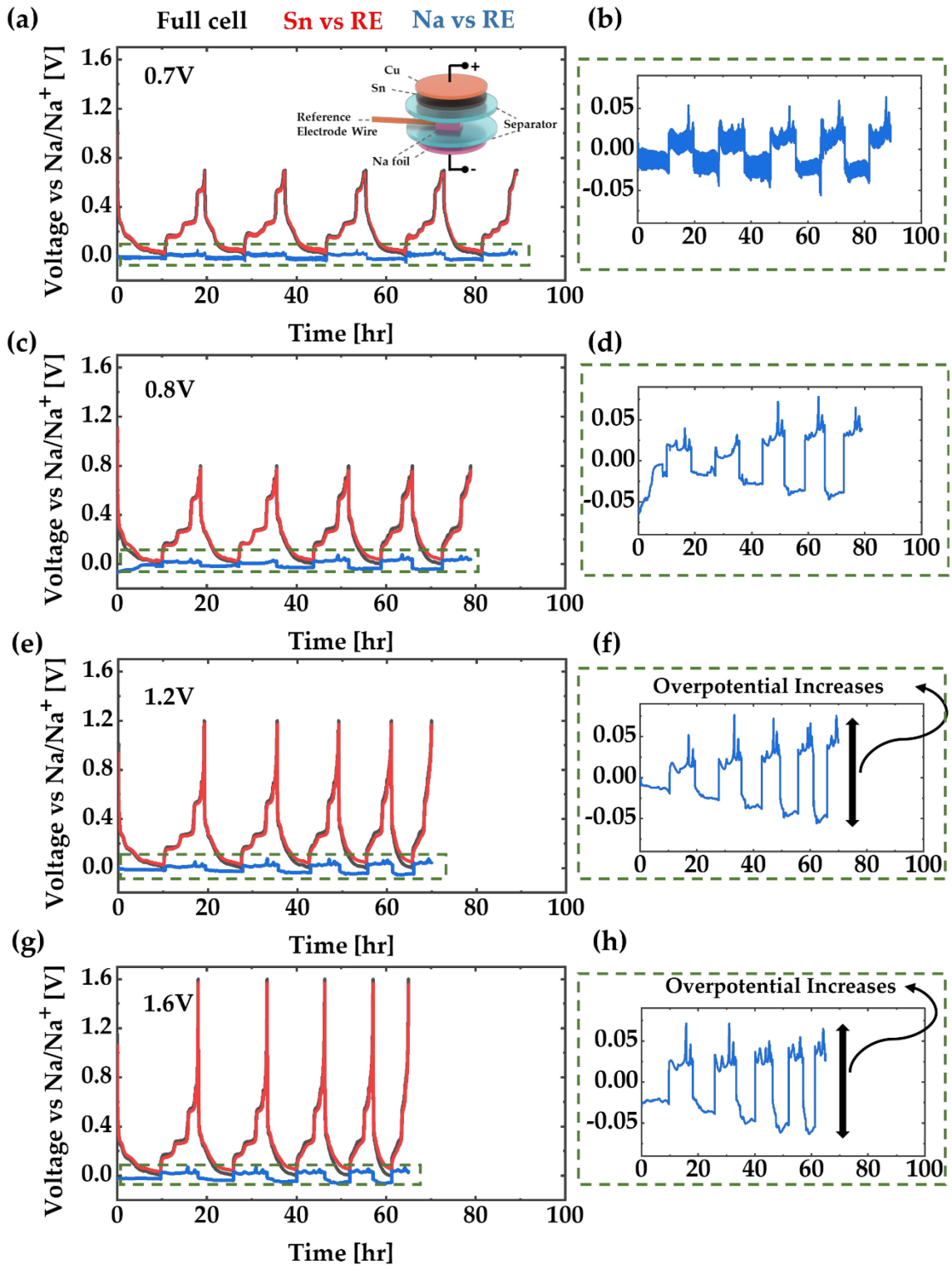

Figure 3. Three-electrode cycling performances of Sn-Na cells in PC electrolyte, discharged and charged to a different cut-off voltages (a)-(b) 0.7V , (c)-(d) 0.8V, (e)-(f) 1.2V and (g)-(h) 1.6V at 0.1 C-rate. Inset of Figure (a) shows the three-electrode cell configuration.

It is arduous to uncouple Na alloying, de-alloying, and plating, stripping with two-electrode, bringing the necessities of using a three-electrode setup to untie the working electrode effect from counter electrode effect. The variation of working electrode potential and counter electrode potential at different cut-off voltages are shown in **Figure 3**. Three electrode cells showed a similar trend as two-electrode cells at higher cut-off potential, showing an initial higher specific capacity followed by a significantly faster capacity decay. The cut-off voltage at 0.7V could guarantee a strong adhesion of a "mud-like" structure with Sn electrode as evident from the SEM images and buffer the volume change during repeatable Na alloying/de-alloying process, subsequently resulting in the long-term stable cycling. To get a more thorough picture of the capacity evolution at different cut-off voltages, we analyzed the progression of the Na-metal electrode overpotential with cycling for the Na-Sn cell. The symmetric cells (Na electrode vs. Na RE (reference electrode)) voltage hysteresis are shown in **Figures 3(b), (d), (f), (h)**. The voltage hysteresis results evinced that the symmetric cells in the presence of the PC electrolyte, using lower cut-off voltage (0.7V), provided stable and low polarization with cycling, indicating lower impedance over Na plating/stripping cycles. However, as we increase the cut-off voltage to 0.8V, 1.2V, and 1.6V, the symmetric cell shows increasing plating-stripping overpotential after five cycles reflecting higher electrolyte and interfacial impedance. This asymmetry in the plating and stripping overpotential where the time difference between the voltage minimum and maximum becomes substantial could not have been recognized from two-electrode cell studies.

The three-electrode impedance analysis for the Na-Sn cells allows for additional in-depth investigation of the reaction mechanisms for the electrodes after five cycles. As shown in **Figure 4(a)**, the impedance for pristine electrode shows one semi-circle and cycled electrodes at different cut-off voltages; similar to the 2-electrode cell, the 3-electrode cell exhibited two high and medium frequency semi-circles linking the Na+ ion migration through the SEI film (R_{SEI}) and the charge-transfer process (R_{ct}), respectively. **Figures 4(b)-(c)** shows the impedance pot of Sn vs. RE (Na metal) and Na vs. RE, respectively. Na vs. RE shows the R_{SEI} value of 64 Ω, 111 Ω, 123 Ω and 165 Ω for 0.7V, 0.8V, 1.2V, and 1.6V, respectively. The increment in the SEI resistance value for Na metal with higher cut-off voltage verifies the voltage stability of Na metal, as observed in **Figure 3**. The value R_{SEI} for Na metal is significantly higher compared to that of Sn electrode and dominates the overall SEI resistance of the full cell. Whereas the value for R_{ct} is quite large for Sn electrode (for e.g., 195 Ω for Sn

and 16 Ω for Na metal at 0.7V cut-off voltage), indicating the dominance of Sn electrode over Na metal during the charge-transfer process.

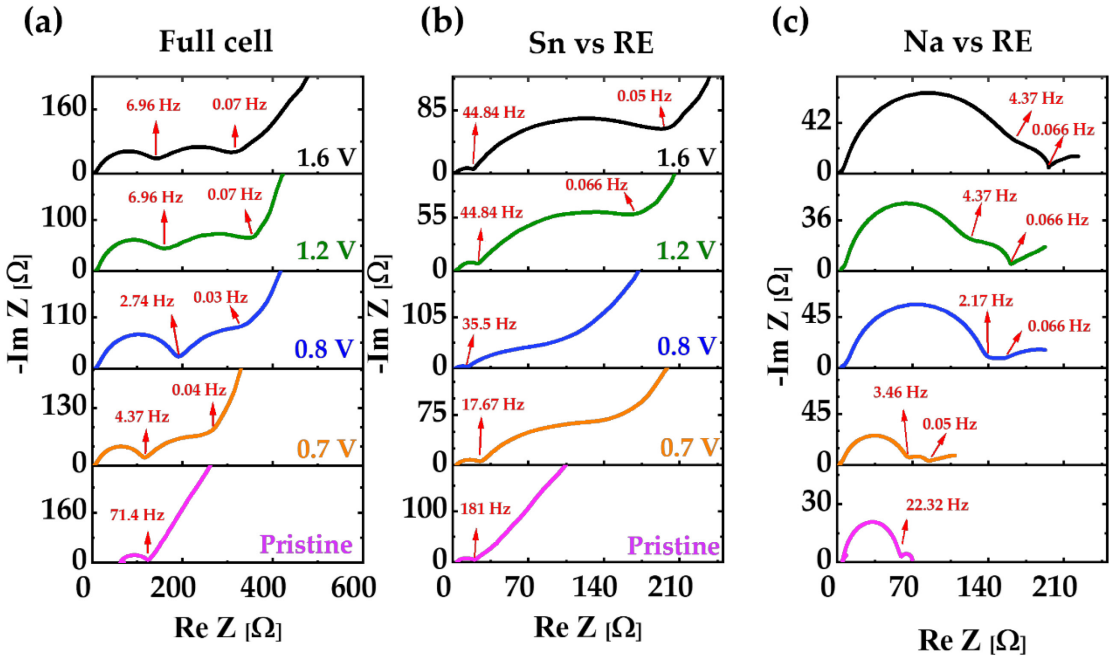

Figure 4. EIS curves of three-electrode Sn-Na cells after 5 cycles at 0.1 C-rate. (a) Full cell, (b) Sn vs. RE (reference electrode), and (c) Na metal vs. RE. In the Na vs. RE case, the two depresses semi-circle is more evident for 1.2 V and 1.6 V.

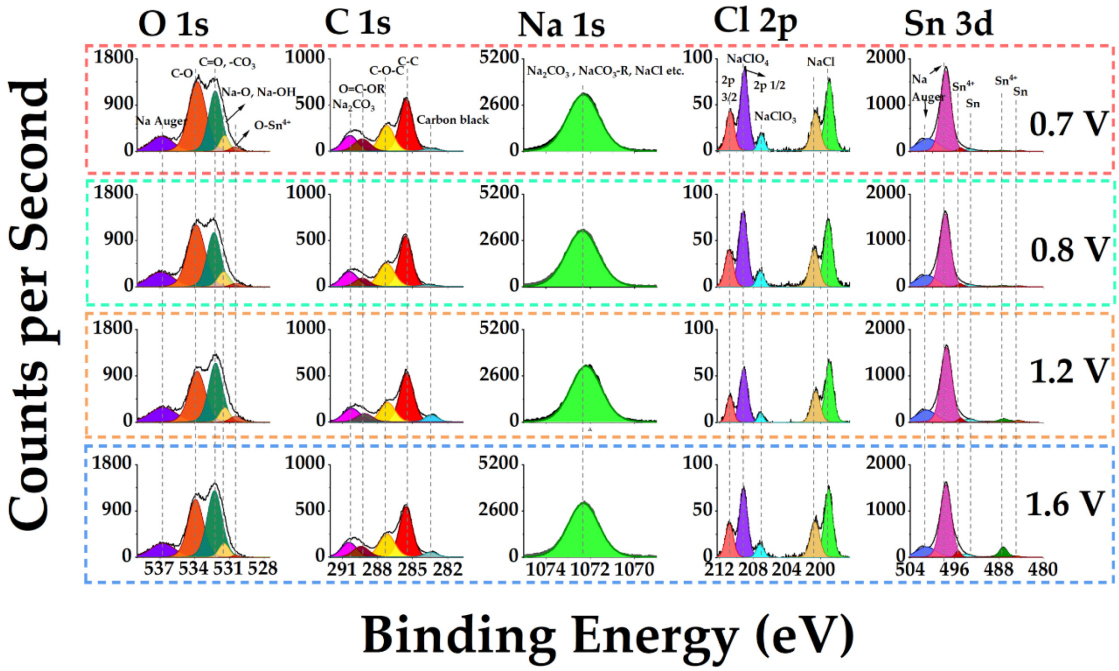

Figure 5. Ex-situ X-ray Photoelectron Spectroscopy (XPS) patterns of the Sn electrode after 20 cycles at different charged states (0.7V, 0.8V, 1.2V, 1.6V).

To confirm the origin of different levels of degradation as evident from the electrochemical performances and to understand how the surface chemistry progresses at a different state of charge, ex situ X-ray Photoelectron Spectroscopy (XPS) was conducted, presented in **Figure 5**. The surfaces of the Sn pristine films are composed of an oxide multilayer made of C, Na, Cl, etc. The XPS binding energies (BE) were calibrated by moving the smallest-BE carbon peak to 285.6 eV, representing C-C bonding. The close examination of the O 1s group shows that the intensity ratio between C-O and C=O changes as we increase the end of charge voltage. The cells charged at lower cut-off voltages (0.7 V and 0.8V) have a higher intensity of C-O peak compared to the C=O peak. However, when the cell was charged to a higher voltage (1.2 V and 1.6 V), the intensity of C=O increases, indicating the strong presence of alkyl carbonates and organic carbonates SEI species (e.g., Na_2CO_3 and $ROCO_2Na$, where R is different long-chain alkyl groups) on the surface. This is also evident from the Energy-dispersive X-ray spectrometer (EDS) analysis shown in **Figure S5**. Higher carbon and oxygen content were detected for the high end of charge voltage (1.6V). The evidence of 530.5 eV in the O 1s core peak suggests the formation of SnO_2. In the case of C 1s, C–O, C=O, and O–C(O)–O (carbonate) bonds were present in all the spectra. The peak intensity associated with carbon black was more pronounced for 1.2 V and 1.6 V cases, which primarily indicates the dissolution of the thick SEI layer and exposure of fresh electrodes. For the Na 1s case, all the cases have similar peak intensity and broadening. The electrode surface was washed several times with PC solvent to eliminate the excess Na salt. However, Chlorine ($NaClO_4$, $NaClO_3$, and NaCl) was still detected at the surface are either from electrolyte salt or from degraded products of electrolyte. NaCl is formed spontaneously at the very beginning of cell preparation and later suppressed by dominant organic and inorganic SEI components. The surface film of the electrode with the lower end of charge voltages has a higher intensity of $NaClO_3$ compared to the higher end of charge voltages. The evidence of Sn in the surfaces was surprisingly suppressed when we charged the cell at 0.7 V and 0.8 V. This indicates that a thick electrode-electrolyte "interface" layer (>5-10nm) is molded on the surface of the electrode, which is greater than the probing depth of XPS.[36,37] Sn is prominently detected at 1.2 V and 1.6 V, suggesting interface layer dissolution or removal (**Figure S6**). This is predominantly due to the uncontrollable volume changes induced during the almost complete Na de-insertion process. The two peaks at 494.2 ($3d_{5/2}$) and 484.5 eV ($3d_{3/2}$) corresponds to metallic β-Sn (Sn^0), and the other two peaks at 495.4 and 487.26 eV links to SnO_2 resulted from the oxidation of the Sn particles surface (Sn^{4+}).[38–41] Due to the strong interaction between Sn and SnO_2, the binding energy of Sn^0 and Sn^{4+} shifted to a higher position.[42] XPS analysis visibly conveys that

variation in surface conditions due to cut-off voltages plays a vital role in determining the nature of electrode-electrolyte interphase.

Electrochemical and morphological analysis of Sn anodes with FEC electrolyte

Fluro ethylene carbonate (FEC) is well accepted in metal batteries, imparting flexibility to the SEI layer and accommodating large volume changes. To examine the reversibility of the sodium alloying/de-alloying process for the FEC protected electrodes, galvanostatic cycling experiments were conducted with the corresponding Na-Sn half-cells at different cut-off voltages (see **Figure 6(a)**). In the presence of FEC, the first discharge capacity is much less than the PC electrolyte, which is similar to the one reported in the literature.[43] The similar observation has been seen for Sn-based composite electrodes in the presence of FEC additives that FEC shows lower capacity at first but stabilizes the cycling performance over time.[44] Excess FEC might be the reason behind the limited capacity during the first cycle. The leftover FEC, which was not absorbed during the first SEI layer formation, will continue to repair the layer until it is depleted. During the repair process, it binds with Na, preventing it from contributing to charge exchange, causing the undesirable loss of capacity.[45] Interesting to us was that the discharge/charge capacity does not strongly depend on the cut-off voltage in the presence of FEC. The first charge and discharge capacity of all the cells were significantly lesser than the PC-based electrolyte. However, all the cells show excellent capacity retention. When the cell was charged to higher voltages (1.2V and 1.6V), charge and discharge capacities were quite unstable, indicating the occurrence of passivation deposition and dissolution process.

Figure 6(b) shows the Coulombic Efficiency of Na-Sn cells with FEC electrolyte additive. The CE at the first cycle was 55.4%, 65.08%, 68.48% and 69.87% for the 0.7V, 0.8V, 1.2V and 1.6V, respectively. First, these results clearly show that FEC-containing electrolyte has less CE than only PC-based electrolyte, which is mostly due to the consumption of additional electrolyte; however, the reversibility is much better. Whether the addition of FEC to a carbonate-based electrolyte enriches or impairs the initial CE, contrasting views exist in literature.[46,47] After 20 cycles, the CE was 99.54%, 99.03%, 97.05% and 96.53% for the 0.7V, 0.8V, 1.2V and 1.6V, respectively. It seems that cycling at a lower cut-off voltage has higher CE than a higher cut-off voltage.

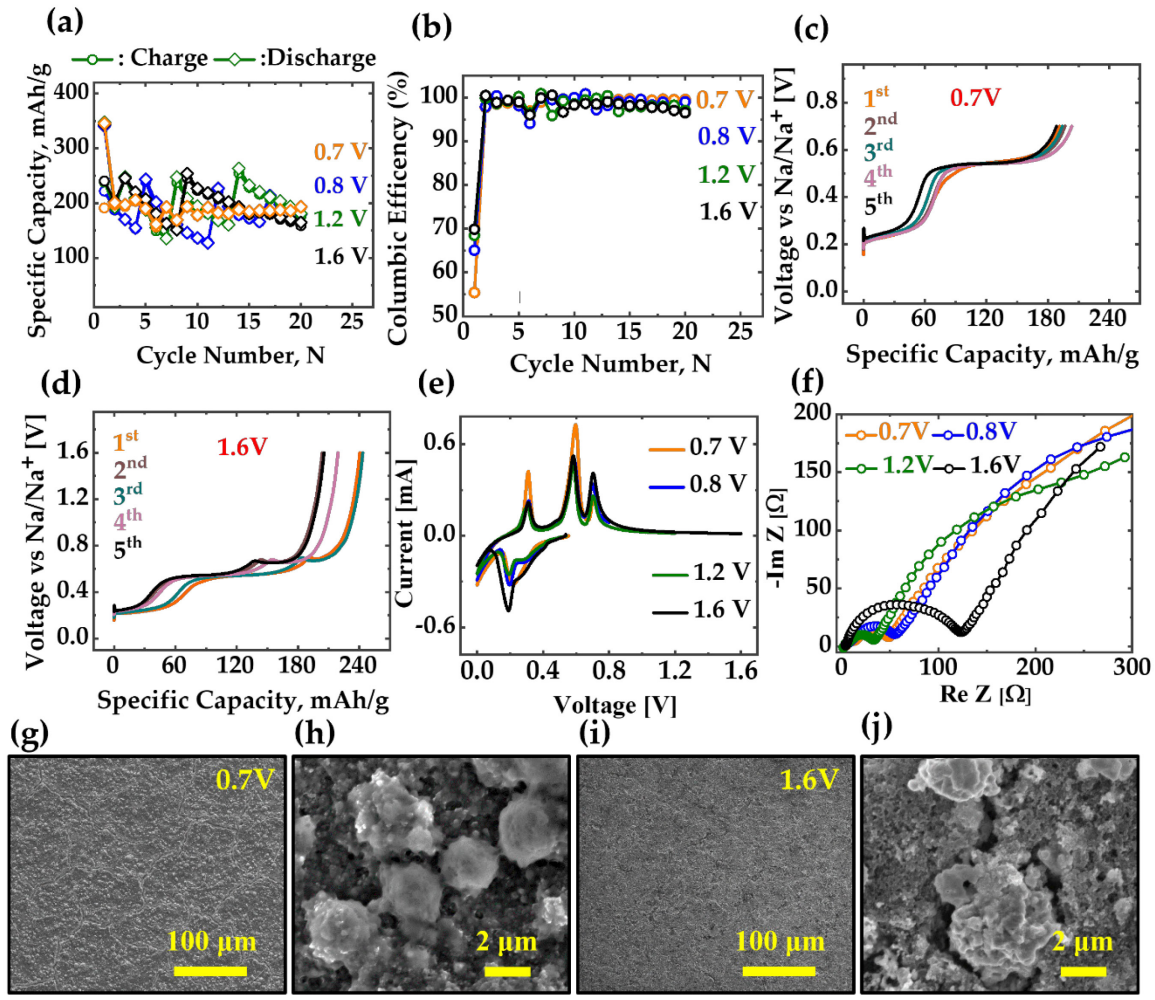

Figure 6. The Sn-Na cells were discharged and charged to different cut-off voltages in the presence of an FEC electrolyte additive. The cycling was done at a 0.1 C-rate for the first 5 cycles, then at a 0.2 C-rate for the next 15 cycles. (a) Specific Capacity vs. Cycle number, (b) Columbic efficiency vs. cycle number. First 5 charge profiles for (c) 0.7 V and (d) 1.6 V. (e) Cyclic voltammetry of cells after 1 cycle (0.1 C-rate) (f) EIS after 20 cycles at different cut-off voltages. SEM images of Sn electrode after 20 cycles at (g)-(h) 0.7 V and (i)-(j) 1.6 V.

Figures 6(c)-(d) compares the typical charge voltage profiles for the cells at different cut-off voltages. According to the voltage profiles, 0.7 V shows only two plateaus, whereas 1.6 V shows an additional plateau after 0.7 V. It was reported earlier that the formation of $Na_{15}Sn_4$ is inhibited by FEC and thus, only 3 plateaus related to the transformation Na_9Sn_4 to NaSn (~0.23 V), NaSn to $NaSn_3$ (~0.54 V) and $NaSn_3$ to Sn (~0.68 V) were observed.[48] Although a slight capacity loss was observed in 5 cycles, the voltage profiles were maintained compared to PC only electrolyte even at a higher cut-off voltage (1.6V). While the separation between the 1st

and 5th charges increased with cut-off voltage, the differences were negligible. The cyclic Voltammetry curve of the cells in **Figure 6(e)** shows better peak reversibility for all the cases than PC-based electrolyte, corroborating the constant current cycling results.

Nyquist impedance diagrams of cycled cells in **Figure 6(f)** consist of two semi-circles, followed by almost a linear frequency variation at low frequencies. The impedance analysis shows a small semi-circle of significantly lower diameter at high frequency and a low-frequency semi-circle with a larger diameter for cycled cells. The size of the semi-circles shrank substantially with the presence of FEC compared to PC suggesting a stable, homogeneous, and thinner SEI layer. Surface film resistance, R_{SEI}, related to the SEI layer, is around 12 Ω, 22 Ω, 16 Ω, 26 Ω for 0.7V, 0.8V, 1.2V and 1.6 V, respectively. R_{ct}, is related to charge transfer, is around 29 Ω, 42 Ω, 32 Ω, 98 Ω for 0.7V, 0.8V, 1.2V and 1.6 V, respectively. Cycling the cells at lower cut-off voltage decreases the charge transfer-related impedance, indicating the stability of morphological features and preservation of the electronic percolation network.[46] The size of the charge transfer-related semi-circles increased significantly with the higher cut-off voltage indicating the kinetic limitation, which can be related to the greater morphological changes of the electrode.

SEM images in **Figures 6(g)-(h)** show that at lower cut-off voltages, particles still maintain the spherical shape. However, when charged to 1.6 V, agglomerated structures can be seen in **Figure 6(i)-(j).** Charging/discharging to deeper cut-off voltage leads to an enormous volume contraction/expansion. A larger amount of Na-ion insertion/de-insertion results in significant volume changes and fractures in electrodes, and with the increase in particle size, their proclivity to form aggregates also increases.[49,50] Low-morphological changes with higher microstructural integrity exist for 0.7V cut-off voltage. The agglomerated particles at 1.6 V have reduced electrochemically active surface area, resulting in poor ionic conductivity and a larger charge transfer impedance loop, as seen in **Figure 6(f)**.

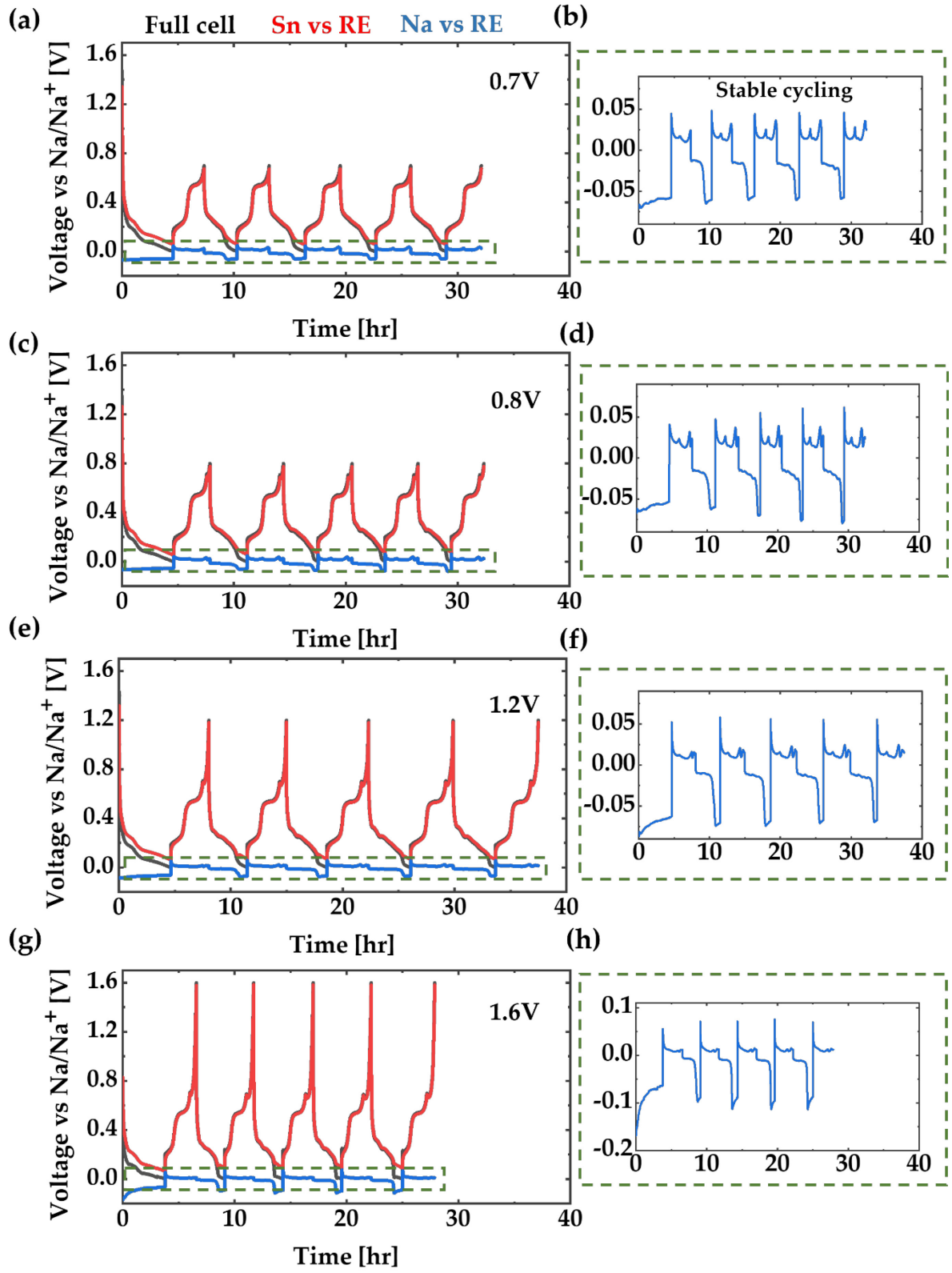

Figure 7. Three electrode cycling performances of Sn-Na cells in PC: FEC electrolyte, discharged and charged to a different cut-off voltage (a)-(b) 0.7V , (c)-(d) 0.8V, (e)-(f) 1.2V and (g)-(h) 1.6V at 0.1 C-rate.

The promising impact of FEC on the performance stabilization of the 2-electrode cell encouraged us to inspect the impact of FEC on Sn electrode and Na metal using a Na reference electrode. The 3-electrode cell in **Figure 7** shows a stable symmetric cell performance (Na metal vs. reference electrode) for all the cut-off voltages. Unlike PC-based electrolyte, FEC-protected Na metal vs. RE showed no changes in overpotential with cycling at all the cut-off voltages. The formation of the FEC-derived stable and robust SEI layer is likely an explanation for the improved Na metal overpotential. In view of this, ameliorating effect of FEC on Na metal anode could be ascribed to the overall enhanced electrochemical performance reversibility of Na-Sn cells.

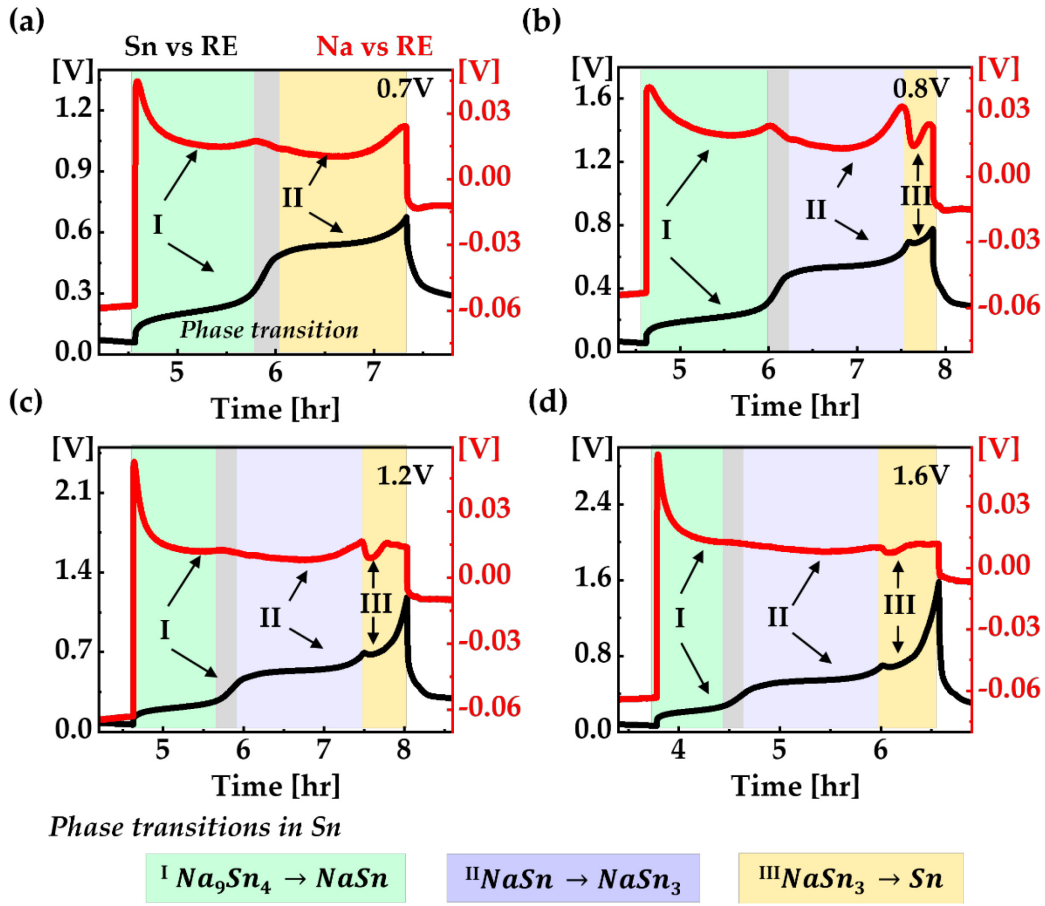

Figure 8. Voltage trace showing the reaction pathways at Sn and Na metal electrode as a function of time obtained from the three-electrode cell study (a) 0.7V, (b) 0.8V, (c) 1.2V, and (d) 1.6V. Different colored shaded areas represent regions of transition between pathways.

Figure 8 presents a comparison of voltage-time profiles for de-alloying of Na from Na_xSn electrode and platting of Na in Na metal. The trends of the Na plating result are of particular

interest here, as it follows the plateaus related to the series of reaction steps in the Sn electrode during Na_xSn to Sn transformation. The voltage traces of Na metal show two different reaction pathways associated with the electrodeposition process, while 0.7V was selected as cut-off voltage. As we increased the cut-off voltage to 0.8V, 1.2V, and 1.6V, an extra reaction pathway was observed, which can be linked to the third plateau of the Na de-alloying reaction in the Sn electrode. The time traces of Na metal voltage profile in the context of alloying materials has been reported for the first time and can be explained as follows. A maximum voltage is observed when the polarity is switched, which can be attributed to the high activation energy barrier associated with the electrodeposition. A sharp decline in polarization signifying a shift in Na nucleation to growth is observed when the cell polarization is reduced as the deposition is ongoing. A local minimum voltage was observed during the plated growth in the Na metal. During the phase transformation of Na_xSn after the first plateau in the de-alloying process started to become kinetically limited, the amount of available Na starts to decrease from the surface of Na metal, leading to an increase in cell resistance. As soon as the next plateau in the Na_xSn transition hits, the polarization of Na metal starts to decrease and leads to a local minimum voltage. The interpretation of these voltage traces related to the Sn electrode and Na metal shows the interdependence of both working and counter electrodes, where kinetically fast and slow processes primarily dominate the transitions in voltages.

3. Conclusion

In this study, using Sn microparticles in sodium-ion batteries as an exemplar system, we reveal the electrochemical properties of Sn electrode, Na metal, and interfacial instability as a function of the operational potential window. This study has led to several critical points of understanding.

(1) It is found that in pure PC electrolyte (without electrolyte additives), operation at a lower end-of-charge voltage (0.7 V and 0.8 V) promotes a 'mat' type thick passivation layer, which is easily disintegrated due to sodiation/desodiation driven volume change of the Na-Sn phases. Due to the presence of a thicker interfacial layer, the coulombic efficiency is unstable throughout cycling. However, it is noteworthy that these electrodes exhibit better cycle life, suggesting a greater degree of morphological preservation and reduced attacks from the harsh electrolyte environment. For an elevated end-of-charge voltage of 1.6 V, the poor survival of the tin anodes to cycling was inevitably connected to both thinning of the passivation layer and lack of mechanical integrity. Interface instability

was more pronounced at higher charge voltages where most of the $Na_{15}S_4$ phase was converted to β-Sn, resulting in severe structural degradation.

(2) For the first time, Sn alloying and de-alloying process was decoupled from the Na metal plating and stripping process in the context of a sodium-ion battery. Three-electrode cell reveals that not only Sn electrode goes through rapid degradation at higher cut-off voltage, but Na metal also suffers from detrimental effects in the devoid of electrolyte additives. The increase in overpotential at Na metal suggests that the Na could not be deposited or stripped readily. It is also plausible that the rise in cut-off voltage might have led to more electrolyte consumption, decreasing the electrolyte's viscosity, thus accelerating Na growth to some degree.

(3) Studies with FEC additives show that in the first cycle, PC/FEC has worse CE than PC due to larger Na consumptions indicating the higher reduction rate of FEC than PC; however, it improved significantly from the 2^{nd} cycle indicating the stabilization of SEI. The lower cut-off voltage showed a reduction in the charge transfer-related impedance loop from the impedance analysis, which could be linked to the sustentation of the electrode morphology.

(4) Additionally, three-electrode analysis shows the efficacy of FEC additive in preserving the SEI layer on the Na-metal surfaces and stabilizing the interfacial and charge-transfer impedances. By shielding the electrode from excess electrolyte consumption, FEC remarkably enhanced the cycling stability.

This study comprehensively suggests that the design and control of electrochemical instability at the interface is a pivotal factor in extending the cyclability of sodium-ion batteries with alloying anodes. The voltage modulation and electrolyte modification presented in this work are effective strategies for improving cell performance, which can be easily adapted in a full cell study or even in other battery chemistries to obtain a long lifespan.

When designing the battery, the question is would you rather your cell have a higher initial capacity or be stable? FEC clearly prolongs the cycling stability even if the price to pay is a slight decrease in initial capacities.

4. Experimental setup

Electrode and Electrolyte Preparation: Tin electrodes with 70 wt.% Sn (10 μm, Sigma Aldrich), 11 wt.% Carboxymethyl Cellulose (CMC) binder (Sigma Aldrich), and 19 wt.%

carbon black (Super C65-TIMCAL) are prepared in the conventional slurry method using DI water and ethanol as solvent. Electrolytes were prepared in a controlled moisture environment (H_2O < 0.1 ppm). Sodium salts ($NaClO_4$) were dried in a vacuum oven for 12 h at 100 °C. Then the dried sodium salts were dissolved in Polycarbonate (Sigma Aldrich) solvent or PC: FEC at 1 M by continuously stirring for 12 hours.

Electrochemical Characterization: Sodium foils served both as a counter electrode and as a reference electrode. A cell was assembled into a CR2032 coin cell format using glass fiber (GF/C). Electrochemical characterizations were conducted at room temperature. Neware cycler was used to run the constant current (CC) test. Biologic was used to do the cyclic voltammetry (CV) and Electrochemical impedance spectroscopy (EIS) test. Potentio EIS (PEIS) was conducted in a frequency range of 1 MHz to 0.1 Hz. CV was tested using Sn as the working electrode and Na foils as both counter and reference electrodes with the scan speed of 0.05 mV/s.

Material Characterization: For characterization, the cycled electrodes were disassembled in the glovebox. The electrodes were washed with PC solvent to clean the salts present on the surface. SEM and EDX in (FEI Nova nanoSEM) were used to see the morphological change and elemental distribution. XPS measurements were performed on Kratos AXIS Ultra DLD Imaging X-ray Photoelectron Spectrometer equipped with Monochromatic Al Ka (1486.6 eV), and Ag La (2984.3 eV) anodes and Non-monochromatic dual anode X-ray gun with Al Ka (1486.6 eV) and Mg Ka (1253.6 eV) operated at pressures below 10^{-8} Torr.

Declaration of Competing Interest

The authors declare that they have no known competing financial interests or personal relationships that could have appeared to influence the work reported in this paper

Acknowledgments

Financial support from the National Science Foundation (Award Number:1805656) is gratefully acknowledged.

Supporting Information

Supporting Information is available.

Additional results such as details of voltage profile, SEM images, Cyclic Voltammetry results, Energy dispersive X-ray spectrometer (EDS), Elemental Mapping, XPS spectra of Sn, Comparisons between specific capacity and impedances in different electrolytes are provided.

References

[1] L. Fan, Q. Liu, S. Chen, Z. Xu, B. Lu, Soft Carbon as Anode for High-Performance Sodium-Based Dual Ion Full Battery, Adv. Energy Mater. 7 (2017) 1–8. https://doi.org/10.1002/aenm.201602778.

[2] X. Yao, Y. Ke, W. Ren, X. Wang, F. Xiong, W. Yang, M. Qin, Q. Li, L. Mai, Defect-Rich Soft Carbon Porous Nanosheets for Fast and High-Capacity Sodium-Ion Storage, Adv. Energy Mater. 9 (2019) 1–9. https://doi.org/10.1002/aenm.201803260.

[3] W. Luo, Z. Jian, Z. Xing, W. Wang, C. Bommier, M.M. Lerner, X. Ji, Electrochemically expandable soft carbon as anodes for Na-ion batteries, ACS Cent. Sci. 1 (2015) 516–522. https://doi.org/10.1021/acscentsci.5b00329.

[4] B. Cao, H. Liu, B. Xu, Y. Lei, X. Chen, H. Song, Mesoporous soft carbon as an anode material for sodium ion batteries with superior rate and cycling performance, J. Mater. Chem. A. 4 (2016) 6472–6478. https://doi.org/10.1039/c6ta00950f.

[5] S. Komaba, W. Murata, T. Ishikawa, N. Yabuuchi, T. Ozeki, T. Nakayama, A. Ogata, K. Gotoh, K. Fujiwara, Electrochemical Na insertion and solid electrolyte interphase for hard-carbon electrodes and application to Na-ion batteries, Adv. Funct. Mater. 21 (2011) 3859–3867. https://doi.org/10.1002/adfm.201100854.

[6] M. Dahbi, T. Nakano, N. Yabuuchi, S. Fujimura, K. Chihara, K. Kubota, J.Y. Son, Y.T. Cui, H. Oji, S. Komaba, Effect of Hexafluorophosphate and Fluoroethylene Carbonate on Electrochemical Performance and the Surface Layer of Hard Carbon for Sodium-Ion Batteries, ChemElectroChem. 3 (2016) 1856–1867. https://doi.org/10.1002/celc.201600365.

[7] F.A. Soto, P. Yan, M.H. Engelhard, A. Marzouk, C. Wang, G. Xu, Z. Chen, K. Amine, J. Liu, V.L. Sprenkle, F. El-Mellouhi, P.B. Balbuena, X. Li, Tuning the Solid Electrolyte Interphase for Selective Li- and Na-Ion Storage in Hard Carbon, Adv. Mater. 29 (2017). https://doi.org/10.1002/adma.201606860.

[8] P. Liu, Y. Li, Y.S. Hu, H. Li, L. Chen, X. Huang, A waste biomass derived hard carbon as a high-performance anode material for sodium-ion batteries, J. Mater. Chem. A. 4 (2016) 13046–13052. https://doi.org/10.1039/c6ta04877c.

[9] L. Fu, K. Tang, K. Song, P.A. Van Aken, Y. Yu, J. Maier, Nitrogen doped porous

carbon fibres as anode materials for sodium ion batteries with excellent rate performance, Nanoscale. 6 (2014) 1384–1389. https://doi.org/10.1039/c3nr05374a.

[10] T. Chen, L. Pan, T. Lu, C. Fu, D.H.C. Chua, Z. Sun, Fast synthesis of carbon microspheres via a microwave-assisted reaction for sodium ion batteries, J. Mater. Chem. A. 2 (2014) 1263–1267. https://doi.org/10.1039/c3ta14037g.

[11] J. Górka, C. Vix-Guterl, C. Matei Ghimbeu, Recent Progress in Design of Biomass-Derived Hard Carbons for Sodium Ion Batteries, C. 2 (2016) 24. https://doi.org/10.3390/c2040024.

[12] X. Zhou, Y.G. Guo, Highly disordered carbon as a superior anode material for room-temperature sodium-ion batteries, ChemElectroChem. 1 (2014) 83–86. https://doi.org/10.1002/celc.201300071.

[13] K.S. Eom, J. Jung, J.T. Lee, V. Lair, T. Joshi, S.W. Lee, Z. Lin, T.F. Fuller, Improved stability of nano-Sn electrode with high-quality nano-SEI formation for lithium ion battery, Nano Energy. 12 (2015) 314–321. https://doi.org/10.1016/j.nanoen.2014.12.041.

[14] S. Wei, S. Choudhury, J. Xu, P. Nath, Z. Tu, L.A. Archer, Highly Stable Sodium Batteries Enabled by Functional Ionic Polymer Membranes, Adv. Mater. 29 (2017). https://doi.org/10.1002/adma.201605512.

[15] L.M.Z. De Juan, I.V.B. Maggay, M.T. Nguyen, W.R. Liu, T. Yonezawa, β-Sn nanorods with active (001) tip induced lif-rich sei layer for stable anode material in lithium ion battery, ACS Appl. Nano Mater. 1 (2018) 3509–3519. https://doi.org/10.1021/acsanm.8b00664.

[16] Y. Lee, H. Lim, S.O. Kim, H.S. Kim, K.J. Kim, K.Y. Lee, W. Choi, Thermal stability of Sn anode material with non-aqueous electrolytes in sodium-ion batteries, J. Mater. Chem. A. 6 (2018) 20383–20392. https://doi.org/10.1039/c8ta07854h.

[17] H. Xie, X. Tan, E.J. Luber, B.C. Olsen, W.P. Kalisvaart, K.L. Jungjohann, D. Mitlin, J.M. Buriak, β-SnSb for Sodium Ion Battery Anodes: Phase Transformations Responsible for Enhanced Cycling Stability Revealed by in Situ TEM, ACS Energy Lett. 3 (2018) 1670–1676. https://doi.org/10.1021/acsenergylett.8b00762.

[18] M. Bai, K. Zhang, D. Du, X. Tang, Y. Liu, H. Wang, M. Zhang, S. Liu, Y. Ma, SnSb

Binary Alloy Induced Heterogeneous Nucleation within the Confined Nanospace: Toward Dendrite-Free, Flexible and Energy/Power Dense Sodium Metal Batteries, Energy Storage Mater. 42 (2021) 219–230. https://doi.org/10.1016/j.ensm.2021.07.032.

[19] H. Xie, W.P. Kalisvaart, B.C. Olsen, E.J. Luber, D. Mitlin, J.M. Buriak, Sn-Bi-Sb alloys as anode materials for sodium ion batteries, J. Mater. Chem. A. 5 (2017) 9661–9670. https://doi.org/10.1039/c7ta01443k.

[20] Y. Kim, Y. Kim, A. Choi, S. Woo, D. Mok, N.-S. Choi, Y.S. Jung, J.H. Ryu, S.M. Oh, K.T. Lee, Tin Phosphide as a Promising Anode Material for Na-Ion Batteries, Adv. Mater. 26 (2014) 4139–4144. https://doi.org/https://doi.org/10.1002/adma.201305638.

[21] M. Bai, Y. Liu, K. Zhang, X. Tang, S. Liu, Y. Ma, Alloying-triggered heterogeneous nucleation for the flexible sodium metallic batteries, Energy Storage Mater. 38 (2021) 499–508. https://doi.org/10.1016/j.ensm.2021.03.033.

[22] J. Qian, Y. Xiong, Y. Cao, X. Ai, H. Yang, Synergistic Na-Storage Reactions in Sn4P3 as a High-Capacity, Cycle-stable Anode of Na-Ion Batteries, Nano Lett. 14 (2014) 1865–1869. https://doi.org/10.1021/nl404637q.

[23] B. Huang, J. Yang, Y. Li, S. Xiao, Q. Chen, Carbon encapsulated Sn-Co alloy: A stabilized tin-based material for sodium storage, Mater. Lett. 210 (2018) 321–324. https://doi.org/10.1016/j.matlet.2017.09.055.

[24] T. Yamamoto, T. Nohira, R. Hagiwara, A. Fukunaga, S. Sakai, K. Nitta, Charge-discharge behavior of Sn-Ni alloy film electrodes in an intermediate temperature ionic liquid for the electrolyte of a sodium secondary battery, Electrochim. Acta. 193 (2016) 275–283. https://doi.org/10.1016/j.electacta.2016.02.059.

[25] T. Yamamoto, T. Nohira, R. Hagiwara, A. Fukunaga, S. Sakai, K. Nitta, Electrochemical behavior of Sn-Fe alloy film negative electrodes for a sodium secondary battery using inorganic ionic liquid Na[FSA]-K[FSA], Electrochim. Acta. 211 (2016) 234–244. https://doi.org/10.1016/j.electacta.2016.06.050.

[26] A. Ponrouch, E. Marchante, M. Courty, J.M. Tarascon, M.R. Palacín, In search of an optimized electrolyte for Na-ion batteries, Energy Environ. Sci. 5 (2012) 8572–8583. https://doi.org/10.1039/c2ee22258b.

[27] P. Bai, X. Han, Y. He, P. Xiong, Y. Zhao, J. Sun, Y. Xu, Solid electrolyte interphase manipulation towards highly stable hard carbon anodes for sodium ion batteries, Energy Storage Mater. 25 (2020) 324–333. https://doi.org/10.1016/j.ensm.2019.10.006.

[28] H.S. Hirsh, B. Sayahpour, A. Shen, W. Li, B. Lu, E. Zhao, M. Zhang, Y.S. Meng, Role of electrolyte in stabilizing hard carbon as an anode for rechargeable sodium-ion batteries with long cycle life, Energy Storage Mater. 42 (2021) 78–87. https://doi.org/10.1016/j.ensm.2021.07.021.

[29] M. Fukunishi, N. Yabuuchi, M. Dahbi, J.Y. Son, Y. Cui, H. Oji, S. Komaba, Impact of the Cut-Off Voltage on Cyclability and Passive Interphase of Sn-Polyacrylate Composite Electrodes for Sodium-Ion Batteries, J. Phys. Chem. C. 120 (2016) 15017–15026. https://doi.org/10.1021/acs.jpcc.6b03459.

[30] Y. Zhu, Z. Qian, J. Song, W. Du, J. Pan, D. Wang, J. Yang, Voltage-Modulated Structure Stress for Enhanced Electrochemcial Performances: The Case of μ-Sn in Sodium-Ion Batteries, Nano Lett. (2021). https://doi.org/10.1021/acs.nanolett.1c00489.

[31] J. Ming, Z. Cao, Y. Wu, W. Wahyudi, W. Wang, X. Guo, L. Cavallo, J.Y. Hwang, A. Shamim, L.J. Li, Y.K. Sun, H.N. Alshareef, New Insight on the Role of Electrolyte Additives in Rechargeable Lithium Ion Batteries, ACS Energy Lett. 4 (2019) 2613–2622. https://doi.org/10.1021/acsenergylett.9b01441.

[32] A.M. Haregewoin, A.S. Wotango, B.J. Hwang, Electrolyte additives for lithium ion battery electrodes: Progress and perspectives, Energy Environ. Sci. 9 (2016) 1955–1988. https://doi.org/10.1039/c6ee00123h.

[33] Y. Yang, J. Xiong, S. Lai, R. Zhou, M. Zhao, H. Geng, Y. Zhang, Y. Fang, C. Li, J. Zhao, Vinyl Ethylene Carbonate as an Effective SEI-Forming Additive in Carbonate-Based Electrolyte for Lithium-Metal Anodes, ACS Appl. Mater. Interfaces. (2019). https://doi.org/10.1021/acsami.8b20706.

[34] E. Quartarone, P. Mustarelli, Review—Emerging Trends in the Design of Electrolytes for Lithium and Post-Lithium Batteries, J. Electrochem. Soc. 167 (2020) 050508. https://doi.org/10.1149/1945-7111/ab63c4.

[35] E. Greco, G. Nava, R. Fathi, F. Fumagalli, A.E. Del Rio-Castillo, A. Ansaldo, S.

Monaco, F. Bonaccorso, V. Pellegrini, F. Di Fonzo, Few-layer graphene improves silicon performance in Li-ion battery anodes, J. Mater. Chem. A. 5 (2017) 19306–19315. https://doi.org/10.1039/c7ta05395a.

[36] L. Bodenes, A. Darwiche, L. Monconduit, H. Martinez, The Solid Electrolyte Interphase a key parameter of the high performance of Sb in sodium-ion batteries: Comparative X-ray Photoelectron Spectroscopy study of Sb/Na-ion and Sb/Li-ion batteries, J. Power Sources. 273 (2015) 14–24. https://doi.org/10.1016/j.jpowsour.2014.09.037.

[37] D. Lemordant, W. Zhang, F. Ghamouss, D. Farhat, A. Darwiche, L. Monconduit, R. Dedryvère, H. Martinez, S. Cadra, B. Lestriez, Artificial SEI for Lithium-Ion Battery Anodes: Impact of Fluorinated and Nonfluorinated Additives, Elsevier, 2015. https://doi.org/10.1016/B978-0-12-800679-5.00008-7.

[38] F. Lu, X. Ji, Y. Yang, W. Deng, C.E. Banks, Room temperature ionic liquid assisted well-dispersed core-shell tin nanoparticles through cathodic corrosion, RSC Adv. 3 (2013) 18791–18793. https://doi.org/10.1039/c3ra43532f.

[39] H. Li, J. Zhang, J. Yi, J. Luo, S. Zhu, L. Sun, J. Xiong, W. Zhu, H. Li, Sn-based deep eutectic solvents assisted synthesis of Sn and SnO2 supported hexagonal boron nitrides for adsorptive desulfurization, Chem. Eng. Res. Des. 144 (2019) 11–18. https://doi.org/10.1016/j.cherd.2019.01.025.

[40] F. Zhang, Y. Lian, M. Gu, J. Yu, T.B. Tang, Static and Dynamic Disorder in Metastable Phases of Tin Oxide, J. Phys. Chem. C. 121 (2017) 16006–16011. https://doi.org/10.1021/acs.jpcc.7b04477.

[41] Z. Chen, M. Zhou, Y. Cao, X. Ai, H. Yang, J. Liu, In situ generation of few-layer graphene coatings on SnO 2-SiC core-shell nanoparticles for high-performance lithium-ion storage, Adv. Energy Mater. 2 (2012) 95–102. https://doi.org/10.1002/aenm.201100464.

[42] H. Ma, K. Teng, Y. Fu, Y. Song, Y. Wang, X. Dong, Synthesis of visible-light responsive Sn-SnO 2/C photocatalyst by simple carbothermal reduction, Energy Environ. Sci. 4 (2011) 3067–3073. https://doi.org/10.1039/c1ee01095f.

[43] K. Dai, H. Zhao, Z. Wang, X. Song, V. Battaglia, G. Liu, Toward high specific

capacity and high cycling stability of pure tin nanoparticles with conductive polymer binder for sodium ion batteries, J. Power Sources. 263 (2014) 276–279. https://doi.org/10.1016/j.jpowsour.2014.04.012.

[44] T. Palaniselvam, C. Mukundan, I. Hasa, A.L. Santhosha, M. Goktas, H. Moon, M. Ruttert, R. Schmuch, K. Pollok, F. Langenhorst, M. Winter, S. Passerini, P. Adelhelm, Assessment on the Use of High Capacity "Sn4P3"/NHC Composite Electrodes for Sodium-Ion Batteries with Ether and Carbonate Electrolytes, Adv. Funct. Mater. 30 (2020) 1–12. https://doi.org/10.1002/adfm.202004798.

[45] Y. Qian, C. Schultz, P. Niehoff, T. Schwieters, S. Nowak, F.M. Schappacher, M. Winter, Investigations on the electrochemical decomposition of the electrolyte additive vinylene carbonate in Li metal half cells and lithium ion full cells, J. Power Sources. 332 (2016) 60–71. https://doi.org/10.1016/j.jpowsour.2016.09.100.

[46] J.S. Park, C.L. Margez, T.A. Greszler, Effect of Particle Size and Electronic Percolation on Low-Temperature Performance in Lithium Titanate-Based Batteries, ACS Omega. 4 (2019) 21048–21053. https://doi.org/10.1021/acsomega.9b02393.

[47] V. Etacheri, O. Haik, Y. Goffer, G.A. Roberts, I.C. Stefan, R. Fasching, D. Aurbach, Effect of fluoroethylene carbonate (FEC) on the performance and surface chemistry of Si-nanowire li-ion battery anodes, Langmuir. 28 (2012) 965–976. https://doi.org/10.1021/la203712s.

[48] T. Li, U. Gulzar, X. Bai, M. Lenocini, M. Prato, K.E. Aifantis, C. Capiglia, R. Proietti Zaccaria, Insight on the failure mechanism of sn electrodes for sodium-ion batteries: Evidence of pore formation during sodiation and crack formation during desodiation, ACS Appl. Energy Mater. 2 (2019) 860–866. https://doi.org/10.1021/acsaem.8b01934.

[49] P. Barai, Z. Feng, H. Kondo, V. Srinivasan, Multiscale Computational Model for Particle Size Evolution during Coprecipitation of Li-Ion Battery Cathode Precursors, J. Phys. Chem. B. 123 (2019) 3291–3303. https://doi.org/10.1021/acs.jpcb.8b12004.

[50] J. Wang, C. Eng, Y.C.K. Chen-Wiegart, J. Wang, Probing three-dimensional sodiation-desodiation equilibrium in sodium-ion batteries by in situ hard X-ray nanotomography, Nat. Commun. 6 (2015). https://doi.org/10.1038/ncomms8496.

Supporting Information

Synergistic Voltage and Electrolyte Mediation Improves Sodiation Kinetics in µ-Sn Alloy-anodes

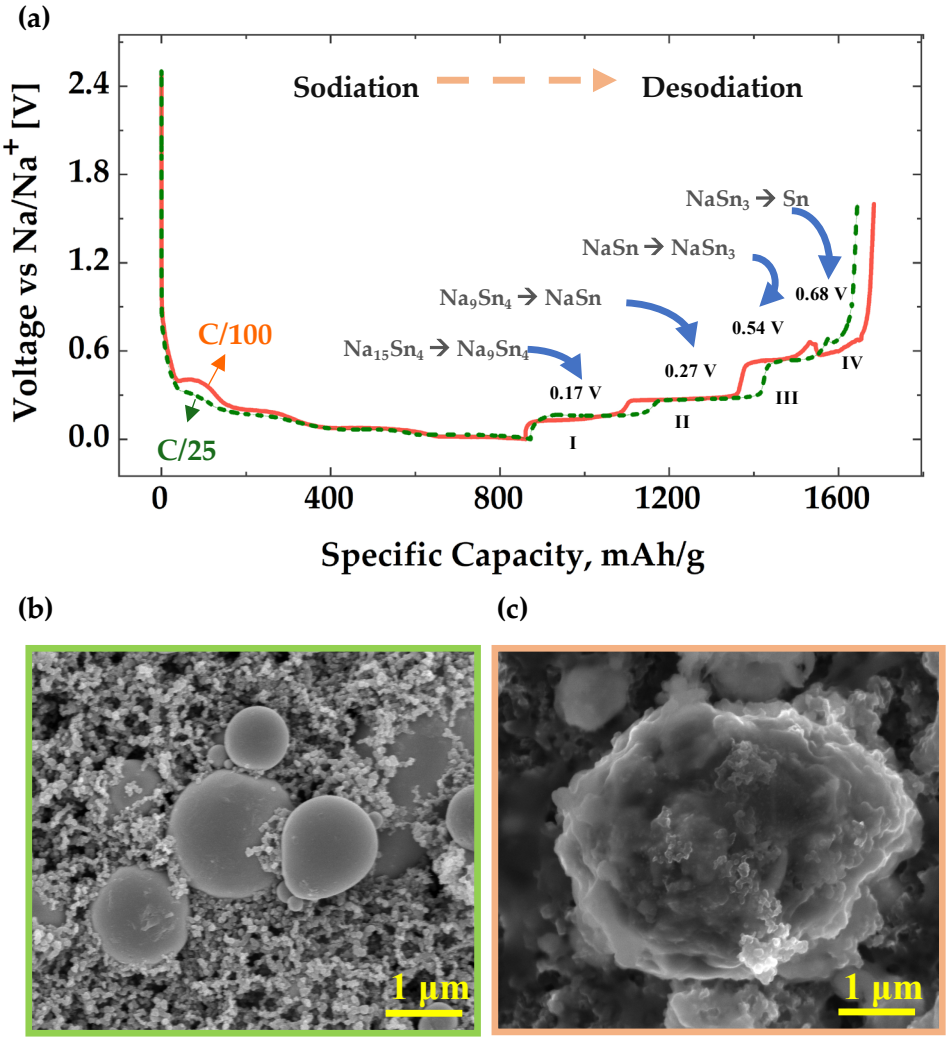

Figure S1: (a) 1st charge-discharge profile of Sn electrode at different current rates (C/25 and C/100). SEM images of (b) fresh and (c) cycled electrodes.

The sloping discharge plateaus are observed at 0.3211V, 0.1748V, 0.0651V, 0.0316V for C/25 and at 0.4061V, 0.2074V, 0.0744V, 0.0176 V for C/100, respectively. During the first desodiation, the plateaus are near 0.1605V, 0.2737V, 0.5422V, 0.6581V and 0.1323V, 0.2752 V, 0.5391V, 0.5747 V for C/25 and C/100, respectively. [1]

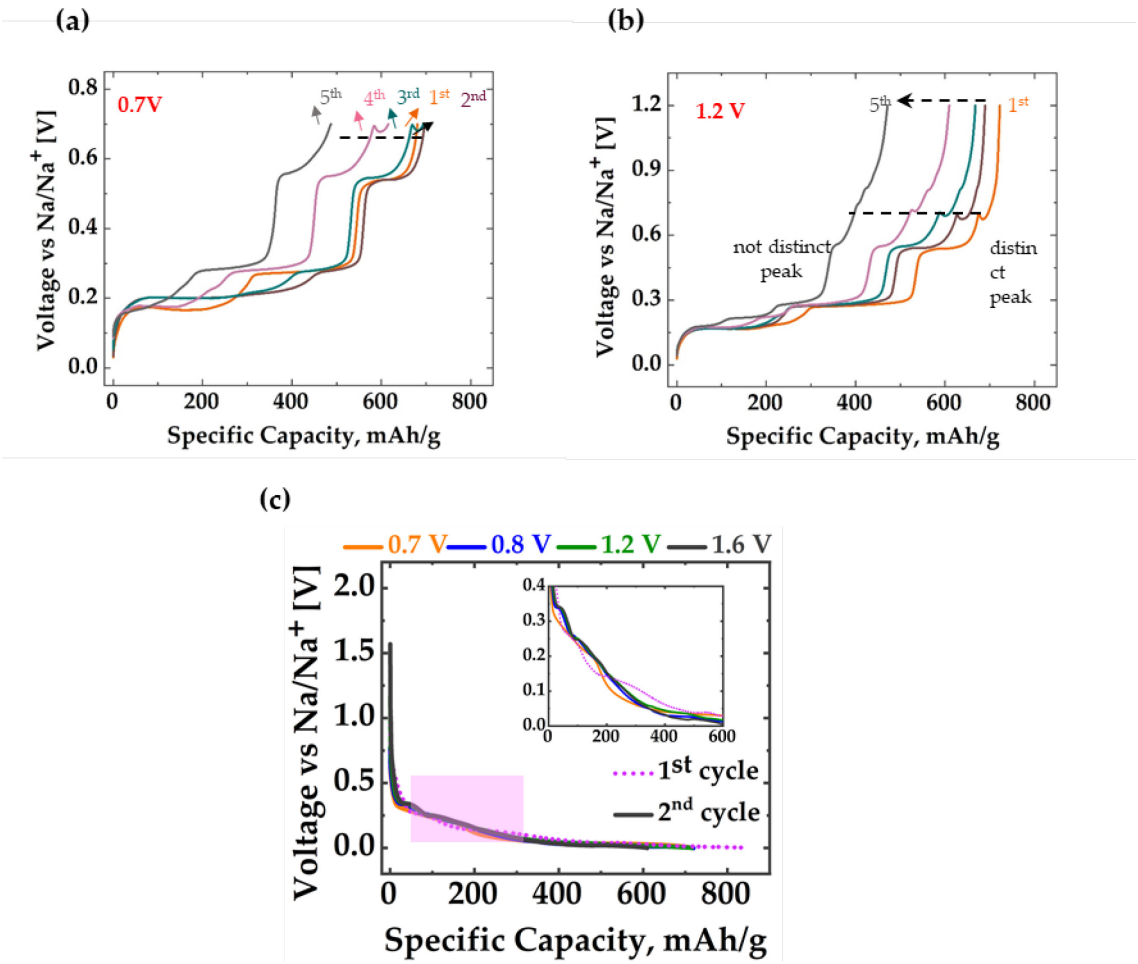

Figure S2. Effect of charge cut-off voltage on cycle performance. The test cells were discharged and charged at constant current at 0.1C-rate to different cut-off voltages for the first 5 cycles. Corresponding charge curves for (a) 0.7 V and (b) 1.2 V. (c) 1st and 2nd discharge profiles for all of the end of charge voltages

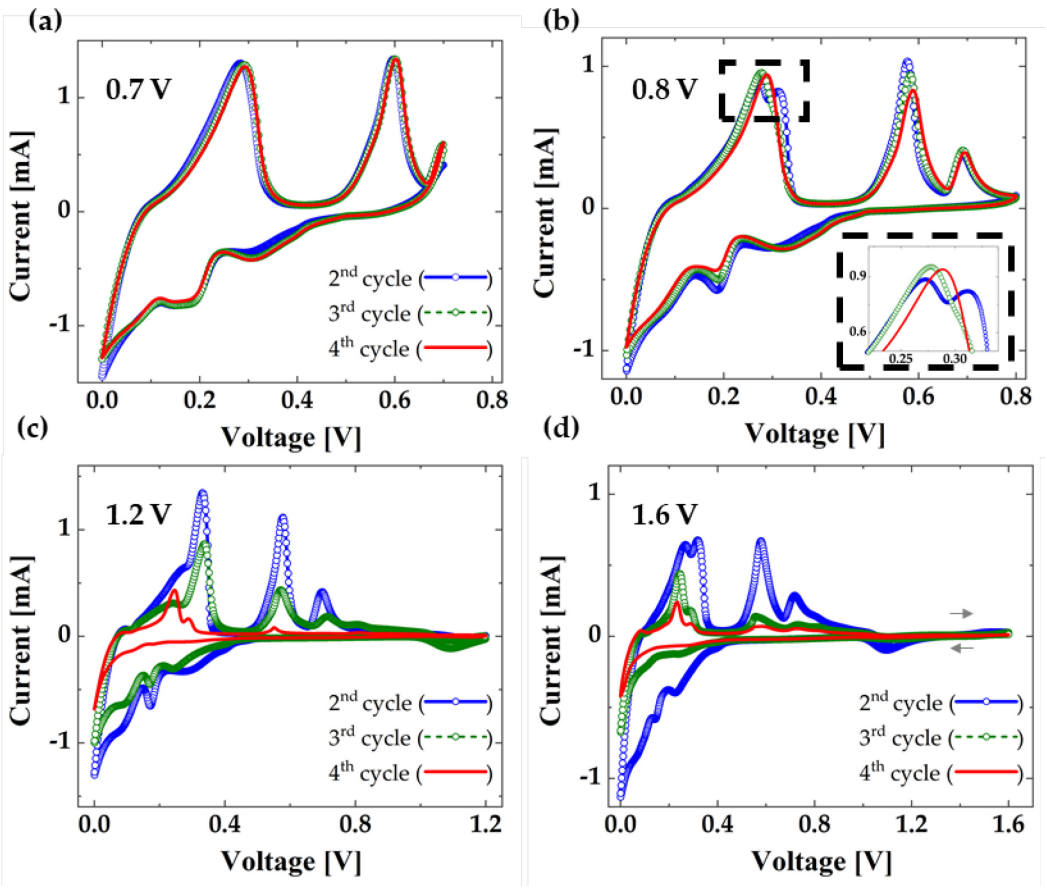

Figure S3: Cyclic voltammetry curves of a fresh Sn-Na cells at different cut-off voltages. (a) 0.7V, (b) 0.8V, (c) 1.2V and (d) 1.6V. (e) CV of cycled Sn-Na cells. This CV test was done after 1 constant current cycle (charge-discharge) at different cut-off voltages.

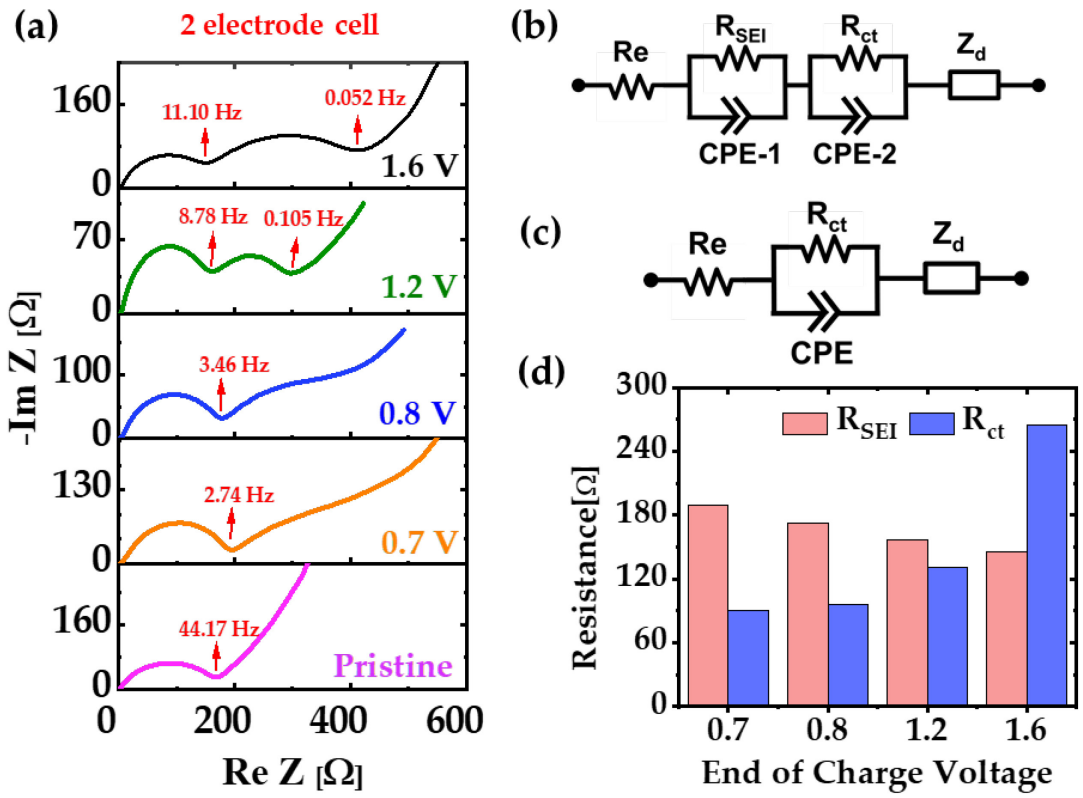

Figure S4. (a) EIS curves of 2-electrode Sn-Na cells after 20 cycles. Equivalent circuits of (b) cycled electrodes and (c) a pristine electrode. (d) Resistance values from EIS circuit fitting for the cycled electrodes.

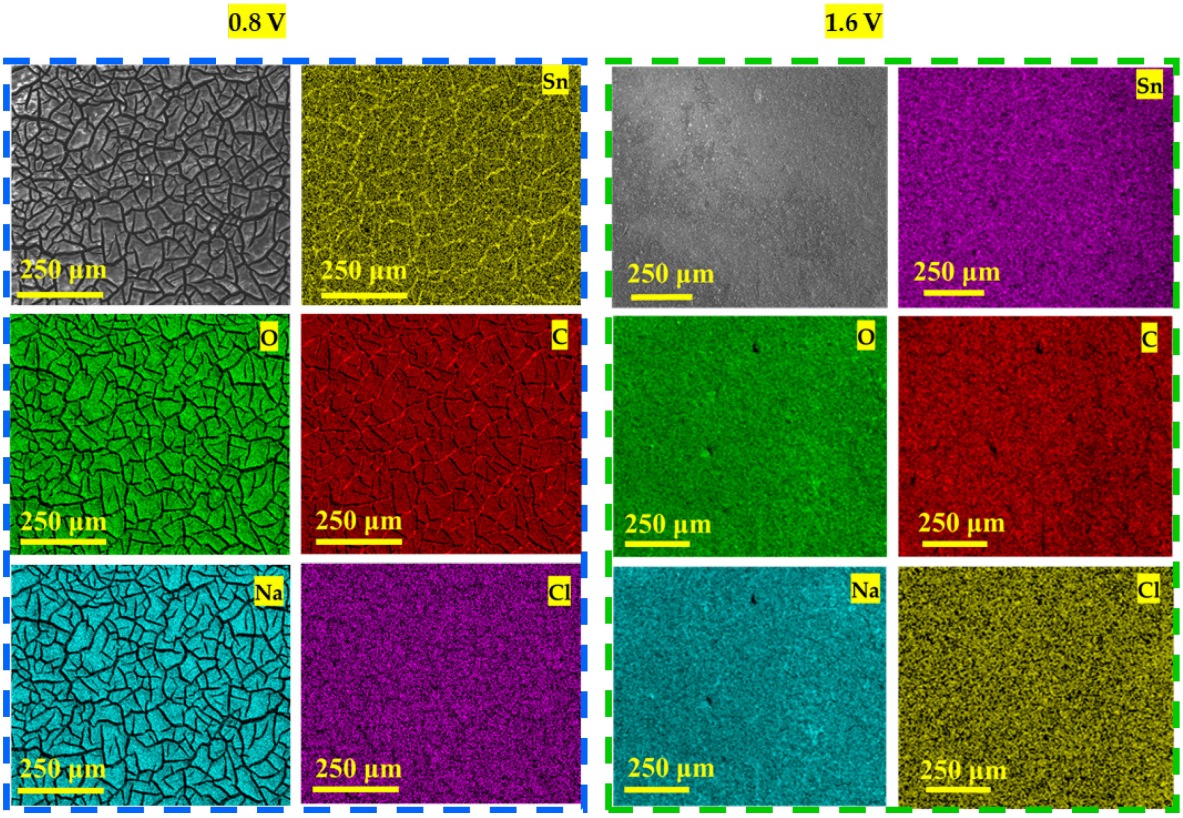

Figure S5: Energy dispersive X-ray spectrometer (EDS) elemental mapping of an Sn electrode obtained from Sn-Na cells cycled at **(a)** 0.8 V and **(b)** 1.6 V.

0.8 V

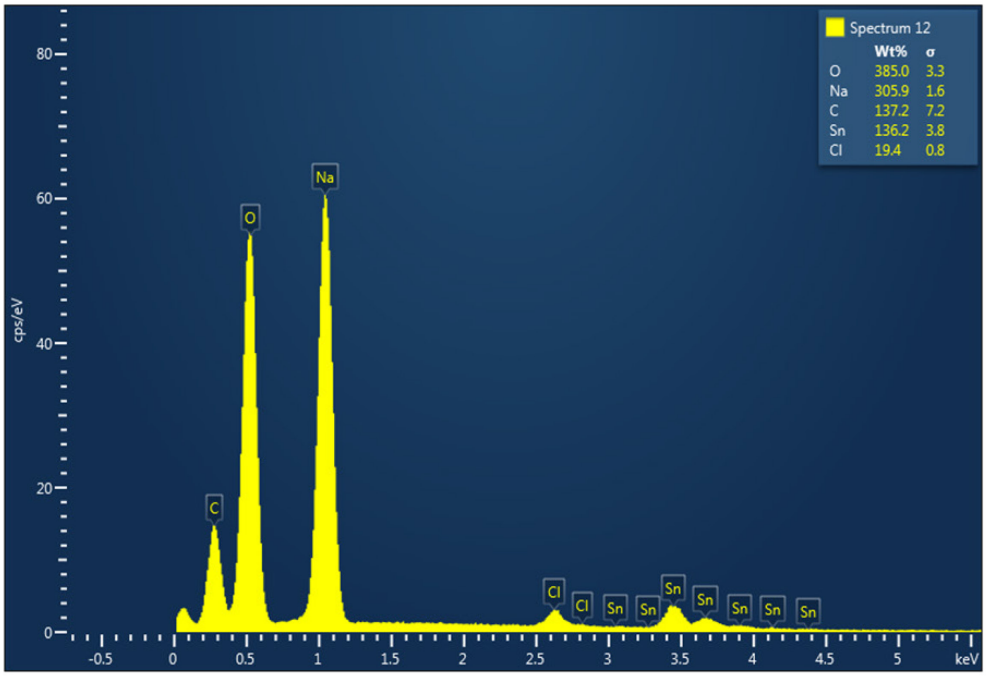

1.6 V

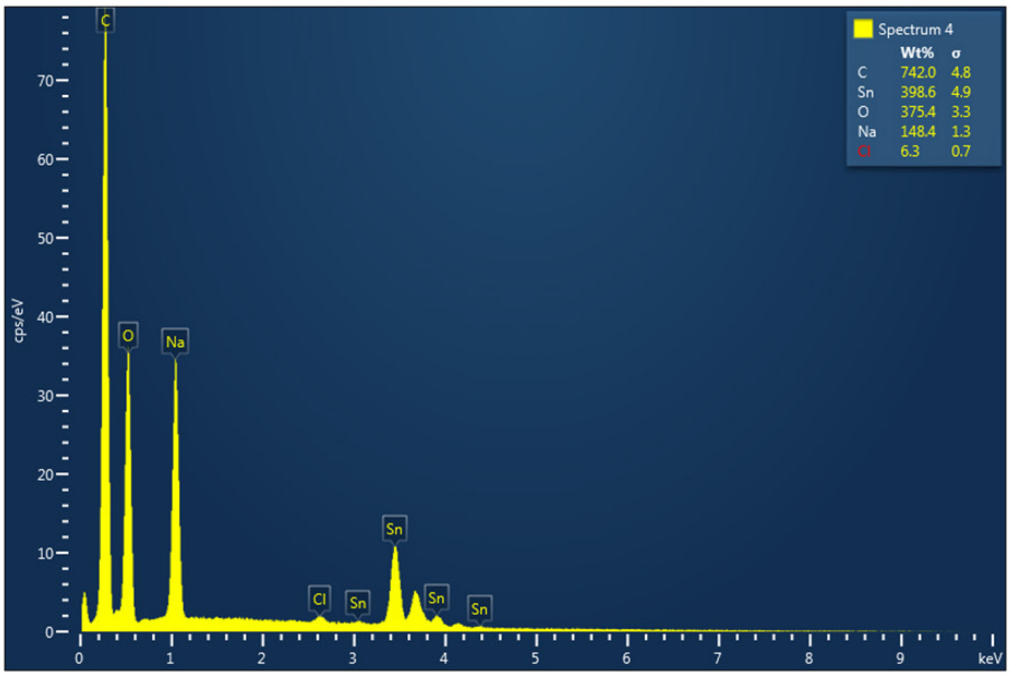

Figure S6: Energy dispersive X-ray spectrometer (EDS) analysis of the electrodes cycled at **(a)** 0.8 V and **(b)** 1.6 V. Area is the same as Fig S4.

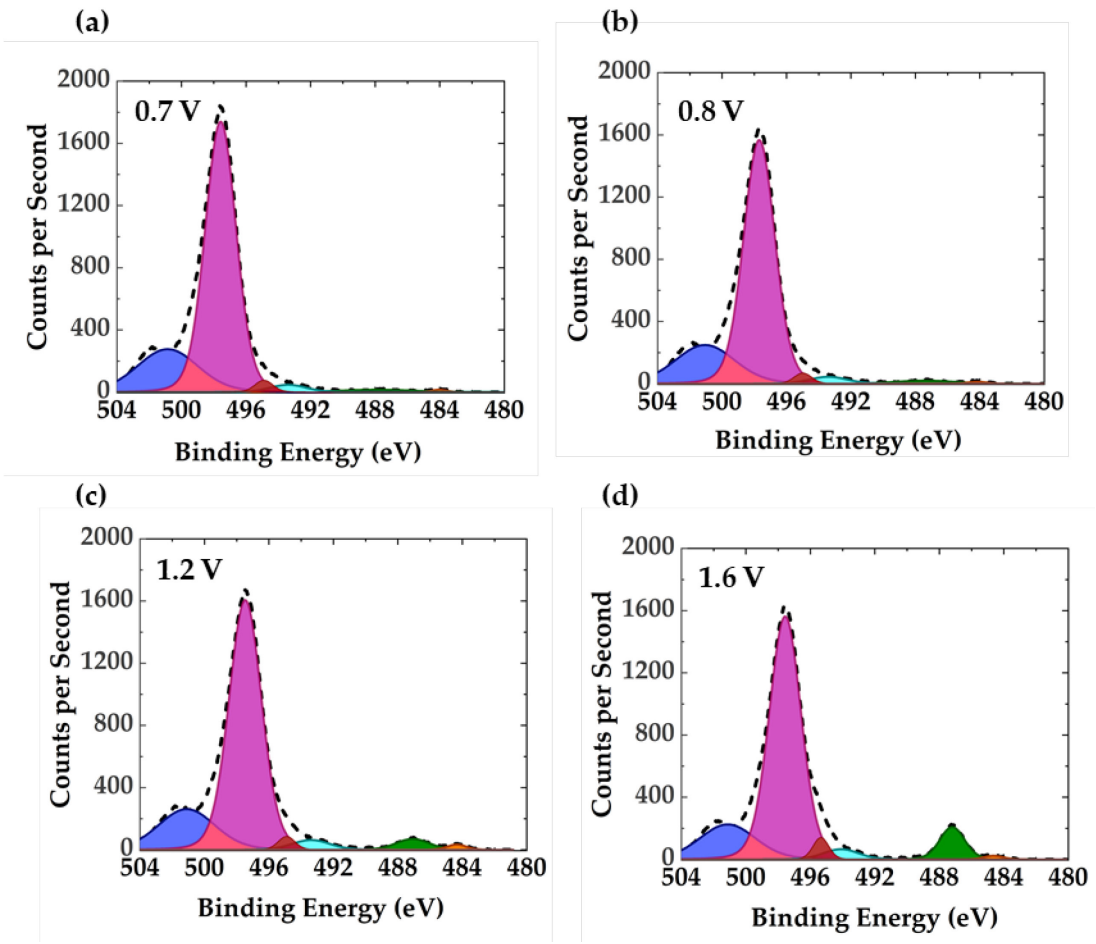

Figure S7: XPS spectra of Sn 3d at different cut-off voltages. (a) 0.7V , (b) 0.8V, (c) 1.2V and (d) 1.6V.

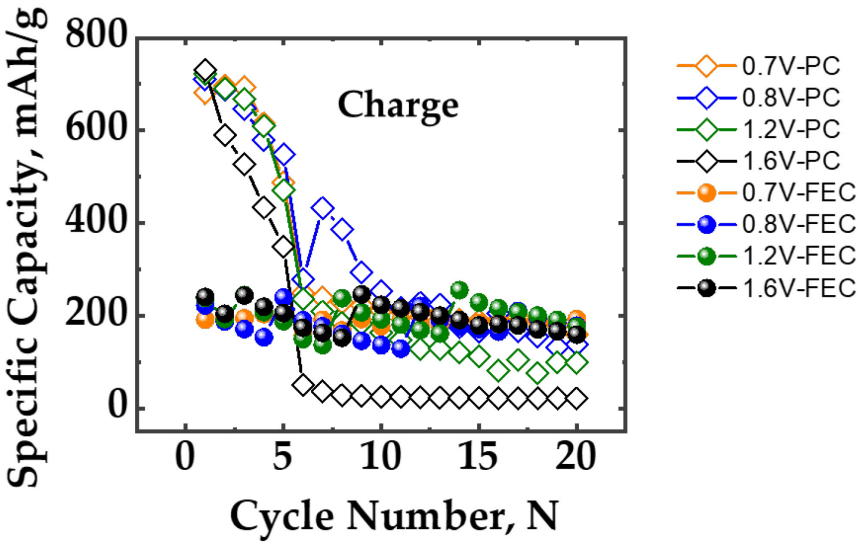

Figure S8: Charge Capacity for the Na-Sn cells at different cut-off voltages with $NaClO_4$ in PC and $NaClO_4$ in PC:FEC electrolyte.

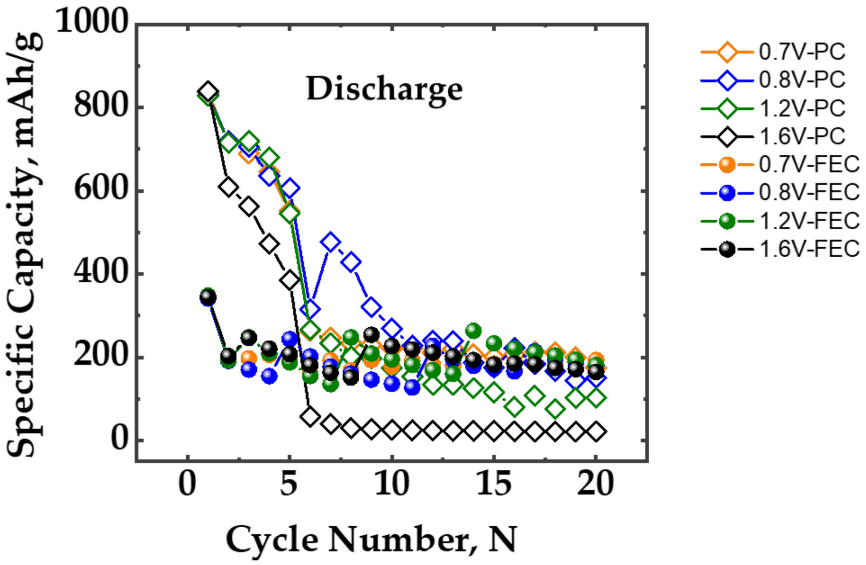

Figure S9: Discharge Capacity for the Na-Sn cells at different cut-off voltages with $NaClO_4$ in PC and $NaClO_4$ in PC:FEC electrolyte.

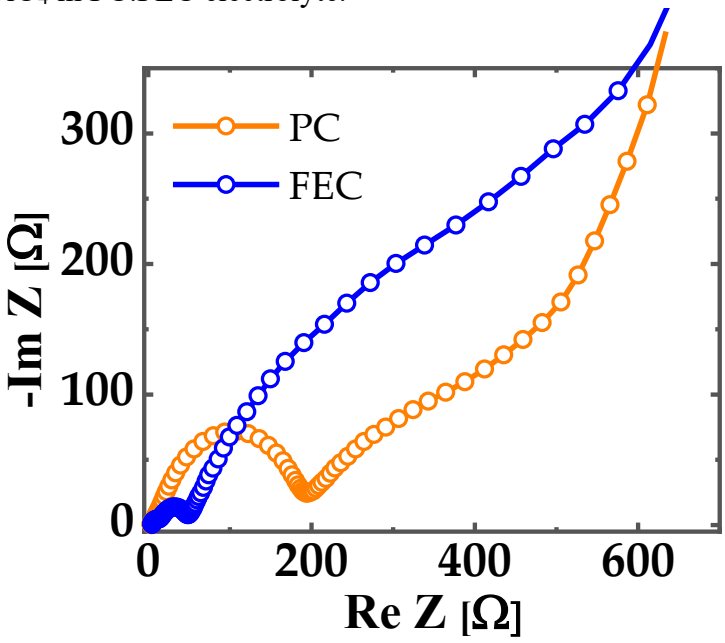

Figure S10: EIS of Na-Sn cells after 20 cycles at different cut-off voltages with $NaClO_4$ in PC and $NaClO_4$ in PC:FEC electrolyte. FEC-based electrolyte shows reduced SEI and charge transfer resistances.

References:

[1] T. Li, U. Gulzar, X. Bai, M. Lenocini, M. Prato, K.E. Aifantis, C. Capiglia, R. Proietti Zaccaria, Insight on the failure mechanism of sn electrodes for sodium-ion batteries: Evidence of pore formation during sodiation and crack formation during desodiation, ACS Appl. Energy Mater. 2 (2019) 860–866. https://doi.org/10.1021/acsaem.8b01934.